Multiparticle scalar dark matter with $\mathcal{Z}_N$ symmetry

Subhaditya Bhattacharya,[*] Lipika Kolay,[†] and Dipankar Pradhan[‡]
Department of Physics, Indian Institute of Technology Guwahati, North Guwahati, Assam-781039, India

(Received 7 May 2025; accepted 29 June 2026; published 4 September 2026)

More than one dark sector particle transforming under the same symmetry provides one stable dark matter (DM) component, which undergoes coannihilation with the heavier particle(s) decaying to DM. Specific assumptions on the kinematics and on the coupling parameters may render the heavier component (s) stable and contribute as DM. The choices of the charges of the dark sector fields under transformation play a crucial role in the resultant phenomenology. In this paper, we systematically address the possibility of obtaining two scalar DM components under $\mathcal{Z}_N$ symmetry. We consider both the possibilities of DM being weakly interacting massive particles (WIMPs) or pseudofeebly interacting massive particles (pFIMPs). We elaborate upon the $\mathcal{Z}_3$ symmetric model, confronting the relic density-allowed parameter space with the recent most direct and indirect search bounds and prospects. We also highlight the possible distinction of the allowed parameter space in single component and two-component cases as well as between WIMP-WIMP and WIMP-pFIMP scenarios.

DOI: 10.1103/yq9j-bh5n

I. INTRODUCTION

What constitutes the nonluminous dark matter (DM) prevailing in the Universe is one of the most critical questions today [1,2]. Different astrophysical and cosmological observations have confirmed its existence [3–12] and suggested that DM constitutes around 26.8% of the total energy budget expressed in terms of relic density, $\Omega_{\rm DM}h^2 = 0.1200 \pm 0.0012$ [13], although a laboratory detection is still awaited. Absent a suitable candidate, the Standard Model (SM) of particle physics needs to be augmented to realize the presence of DM. The broad characteristics associated with DM are being massive, stable, and having no (or feeble) electromagnetic interactions. Other properties remain unconstrained, giving rise to a plethora of possibilities. In this article, we focus on multiparticle DM. Such frameworks are motivated by several phenomenological advantages; the most important one stems from the fact that they allow depletion of DM via interaction between two dark sector particles, which helps alleviate direct, indirect, and collider search limits. There is almost no constraint on multipartite features of the DM sector, except for the collisionlessness of DM particles, coming from Bullet cluster/Abell cluster observations, $\frac{\sigma}{m_{\rm DM}} \lesssim 1\ {\rm cm}^2/{\rm gm}$ [14–17].

In order to satisfy the relic density observed by the anisotropies in Cosmic Microwave Background Radiation (CMBR) experiments, the DM needs to be stable at the scale of the Universe's age. The stability of a fundamental particle is governed by an unbroken symmetry. The lightest dark particle transforming under a symmetry (discrete or continuous) does not possess any tree- or loop-level decay terms with the visible sector. Then, ideally, for having two stable DM particles, two different symmetries are required. However, it is also possible to have one long lived DM component, where the decay terms are assumed to be very small, and the lifetime is larger than the age of the Universe, which does not necessitate a protection via symmetry. However, the large decay lifetime requires either a kinematic suppression or the couplings involved in the process to be small or both. We study such possibilities here with a single $\mathcal{Z}_N$ $(N = 2, 3, 4, \ldots)$ symmetry, where the heavier dark sector particle is long lived and serves as the second DM component. Our intention is to bring out the consequent phenomenology in such cases, especially their implications in direct and indirect search aspects.

DM classification is mostly done based on its production mechanism, whether it remains in thermal bath or out of equilibrium, leading to possibilities like the thermal weakly interacting massive particle (WIMP) [18,19], nonthermal feebly interacting massive particle (FIMP) [20–25], strongly interacting massive particle (SIMP) [26–34], etc. In multicomponent DM frameworks, one can have all kinds of combinations, like WIMP-WIMP [35], WIMP-FIMP [36,37], WIMP-SIMP, SIMP-SIMP [38,39],

[*]Contact author: subhab@iitg.ac.in
[†]Contact author: klipika@iitg.ac.in
[‡]Contact author: d.pradhan@iitg.ac.in

Published by the American Physical Society under the terms of the Creative Commons Attribution 4.0 International license. Further distribution of this work must maintain attribution to the author(s) and the published article's title, journal citation, and DOI. Funded by SCOAP³.

FIMP-FIMP [40,41], etc. In recent studies [42,43], we showed that DM having feeble interaction with the visible sector can thermalize and freeze out via interaction with another thermal DM component, called a pseudofeebly interacting massive particle (pFIMP) [42]. pFIMPs have some distinguishable phenomenological features. In this work, how pFIMPs can arise in multicomponent scenarios having single $\mathcal{Z}_N$ symmetry is addressed. We specifically highlight the cases of $\mathcal{Z}_2$ and $\mathcal{Z}_3$ symmetric scenarios and compare them to $\mathcal{Z}_2 \otimes \mathcal{Z}_2'$ and $\mathcal{Z}_3 \otimes \mathcal{Z}_3'$ models. We show the consequent allowed parameter space of the models goes beyond the so-called Higgs resonance region [42].

Among DM search strategies, the recoil spectrum of detector nucleon (or electrons) in possible scattering with DM via direct detection (DD), the gamma-ray (and antiparticle) spectrum at the galactic center via indirect detection (ID), and the missing energy (or missing transverse momentum) signal at the collider experiments are the major ones. Null results from these experiments so far have imposed bounds on DM parameters, specifically, DM-SM coupling. For example, DD puts a bound on the DM-nucleon/electron scattering cross section as a function of DM mass. As we focus here on the GeV-TeV scale cold DM (which, in turn, supports the structure formation of the Universe), the most relevant DD bounds are obtained from PandaX-4T [44], XENONnT [45], LUX-ZEPLIN [46], DARWIN/XLZD [47], etc. ID provides a bound on the DM self-annihilation and semiannihilation cross section as a function of DM mass; the ones relevant for us come from *Fermi*-LAT [48–50], H.E.S.S [51], and Cherenkov Telescope Array (CTA) [52–55] observations. The relevance of these bounds and search prospects with future sensitivities are scrutinized here in context of the multicomponent DM framework under $\mathcal{Z}_N$ symmetry.

This paper is organized as follows: In Sec. II, we discuss the possibility of getting two stable scalar DM components transforming under a single $\mathcal{Z}_N$ symmetry, and in Sec. III, we discuss briefly the case of $\mathcal{Z}_2$ symmetry. The case pertaining to $\mathcal{Z}_3$ symmetry is elaborated for both WIMP-WIMP and WIMP-pFIMP combinations in Sec. IV. We finally summarize in Sec. V. Appendixes B and D provide some necessary details omitted in the main text.

II. GENERIC DISCUSSION ON TWO-COMPONENT DM UNDER $\mathcal{Z}_N$ SYMMETRY

Two stable DM components require two discrete symmetries, as studied in many different contexts [56–62], while some possibilities of having two DM components using a single discrete symmetry [63–66] have also been discussed. However, a systematic study obtaining all such possibilities under a single symmetry still requires attention. We address it via appropriate assumptions on the coupling parameters of the parent Lagrangian respecting $\mathcal{Z}_N$ symmetry. Our study is limited to scalar DM, while a similar study with vector and/or fermion DM is possible. Similarly, one can also have more than two DM components in a trivial extension of what we present here.

Specifically, we extend the SM with two scalar fields Φ_1 and Φ_2 transforming under a single $\mathcal{Z}_N$ symmetry. The fields Φ_1,Φ_2 might be real or complex, depending on their transformation under the $\mathcal{Z}_N$ symmetry, while Φ_1 and Φ_2 are assumed to be gauge singlets under the SM gauge groups. The lighter component is automatically stable, while the heavier one becomes (kinematically) stable after making some coupling parameters vanishingly small in the nondegenerate case.

In general, the heavier dark sector (DS) particle can have $(n + n')$ body decay, as

$$\text{heavier DS} \to n\,\text{lighter DS} + n'\,\text{SM}, \tag{2.1}$$

with $n, n' = 0, 1, 2, 3\ldots$, and $n + n' \geq 2$; the exact values of $n(n')$ depend on the model. Now, the tree- or loop-level decay of this particle can be stopped by appropriate choices of the model parameters:

(a) For $n' = 0$, the heavier DS particle is stable when

$$n\, m_{\text{lighter}} > m_{\text{heavier}} > m_{\text{lighter}}. \tag{2.2}$$

(b) When $n' \neq 0$, a kinematic condition $n\, m_{\text{lighter}} + n'\, m_{\text{SM}} > m_{\text{heavier}} > n\, m_{\text{lighter}}$ can stop the on-shell decay, but off-shell decays are still possible. The only way to make the heavier DS component stable is to choose appropriate couplings leading to the decay being adequately small, leading to a long lived particle (LLP) DM.

Further, the DM components can be WIMPs, FIMPs, or SIMPs, depending on the strength of their couplings to the SM. The WIMP-WIMP combination is more constrained from direct search than WIMP-FIMP, given that the FIMP is mildly constrained from DD/ID experiments (unless the DM-nucleon/electron scattering occurs via a light mediator). On the other hand, the pFIMP receives milder constraints than the WIMP having feeble DM-SM coupling but still remains accessible for future sensitivities of DD/ID search via WIMP loop, having sizable interaction with WIMP. Therefore, we are more interested in obtaining the WIMP-pFIMP limit of this model, having either the lighter particle or the heavier one as the pFIMP [42,43]. In order to study two-component DM, let us first write the renormalizable scalar potential, $V(\Phi_1, \Phi_2, H)$ (H represents the SM Higgs isodoublet),

$$\begin{aligned} \mathrm{V}(\Phi_1, \Phi_2, H) \supset\ & \lambda_1 |\Phi_1|^2 H^\dagger H + \lambda_2 |\Phi_2|^2 H^\dagger H \\ & + \lambda_3 (\Phi_1 \Phi_2 + \Phi_1 \Phi_2^* + \text{H.c.}) H^\dagger H \\ & + (\lambda_4 \Phi_1^2 + \lambda_5 \Phi_2^2 + \text{H.c.}) H^\dagger H \\ & + V^{\text{int}}(\Phi_1, \Phi_2), \end{aligned} \tag{2.3}$$

where $\lambda_1, \lambda_2, \lambda_3, \lambda_4, \lambda_5$ are dimensionless Higgs portal couplings, and $V^{\rm int}(\Phi_1, \Phi_2)$ contains all possible renormalizable interaction terms (with mass dimensions $\mathcal{M}[2]$, $\mathcal{M}[3]$, and $\mathcal{M}[4]$) between Φ_1 and Φ_2 as

$$\begin{aligned}
\mathcal{M}[2]:&\ \{\Phi_1\Phi_2, \Phi_1\Phi_2^*\} + \text{H.c.};\\
\mathcal{M}[3]:&\ \{\Phi_1|\Phi_2|^2, \Phi_2|\Phi_1|^2, \Phi_1\Phi_2^2, \Phi_1\Phi_2^{*2}, \Phi_1^2\Phi_2, \Phi_1^2\Phi_2^*\} + \text{H.c.};\\
\mathcal{M}[4]:&\ \{\Phi_1^2\Phi_2^2, \Phi_1^2\Phi_2^{*2}, \Phi_1^2|\Phi_2|^2, |\Phi_1|^2\Phi_2^2, |\Phi_1|^2|\Phi_2^2, \Phi_1\Phi_2^3, \Phi_1^*\Phi_2^3, \Phi_1^3\Phi_2,\\
&\ \Phi_1^3\Phi_2^*, \Phi_1\Phi_2|\Phi_1|^2, \Phi_1\Phi_2|\Phi_2|^2, \Phi_1\Phi_2^*|\Phi_1|^2, \Phi_1\Phi_2^*|\Phi_2|^2\} + \text{H.c.}
\end{aligned} \tag{2.4}$$

In Eqs. (2.3) and (2.4), we wrote all possible interaction terms;[1] however, the choice of the symmetry restricts them. It is obvious that if both Φ_1 and Φ_2 contribute as DM, then to prevent the tree-level decay of the heavier component, λ_3 in Eq. (2.3) needs to be sufficiently small[2]; further restrictions arise depending on the possible interaction terms that one can write. If $\Phi_1 \to \omega_N^{q_1}\Phi_1$ and $\Phi_2 \to \omega_N^{q_2}\Phi_2$ under $\mathcal{Z}_N$ symmetry, where $\omega_N^q = e^{i2\pi(q/N)}$ and $q_{1,2}$ define the charges of the fields, then the choice of $q_{1,2}$ also plays a crucial role in deciding the interaction terms, as shown in Table I. The interaction terms are broadly classified into four cases:

$$\begin{aligned}
&(i)\ q_1 = q_2, \text{ and } q_1 + q_2 = N,\\
&(ii)\ q_1 = q_2, \text{ but } q_1 + q_2 \neq N,\\
&(iii)\ q_1 \neq q_2, \text{ but } q_1 + q_2 = N,\\
&(iv)\ q_1 \neq q_2, \text{ and } q_1 + q_2 \neq N.
\end{aligned} \tag{2.5}$$

For the first three cases in Eq. (2.5), we have to consider both kinematic constraints and choose some couplings to be vanishingly small for making the heavy DS particle stable. The heavy DS particles in all these cases decay to SM particles plus DM, falling in the case (b) mentioned before. For the fourth condition in Eq. (2.5), i.e., $q_1 \neq q_2$, and $q_1 + q_2 \neq N$, a two-component DM scenario can arise just by imposing kinematic constraints, as here the decay of the heavy DS particle occurs within the DS *only*, falling into category (a) discussed above; for some example analyses of such scenarios, see [63–68].

Let us take a closer look into the possible terms that one can write involving Φ_1 and Φ_2 depending on their charges under $\mathcal{Z}_N$ transformation, as shown in Table I. The first subrow of Table I shows the case when they have the same charge: $q_1 = q_2 = q$, with $q = N/2$. As q needs to be an integer, this requires N to be even. In such a situation, Φ_1 and Φ_2 can be two real scalar fields, and only a select few terms are allowed amid all the possibilities listed in Eq. (2.4). The second subrow in Table I shows the possible terms when $q_1 = q_2$, but $q_1 + q_2 \neq N$, which restricts us from writing the $\Phi_1\Phi_2$ term, but retaining a term like $\Phi_1\Phi_2^*$ is possible, allowing complex scalar fields only. It is obvious but worth remembering that the complex conjugate fields possess $-q_i$ charges as $\Phi_i^* \to \omega_N^{q_i *}\Phi_i^*$ under $\mathcal{Z}_N$. Furthermore, terms like $\Phi_{1,2}^3$ can be written only if $\frac{3q}{N}$ is an integer, i.e., $\frac{3q}{N} \in \mathbb{N}$, where $\mathbb{N}$ denotes the set of integer numbers. The third and fourth subrows show the interaction terms in the $q_1 \neq q_2, q_1 + q_2 = N$, and $q_1 \neq q_2, q_1 + q_2 \neq N$ cases, respectively. The restrictions that apply in writing the interaction terms are mentioned in the subscript of the parenthesis. For example, the $\Phi_1^m\Phi_2^n$ term can be written for $q_1 \neq q_2, q_1 + q_2 \neq N$ case only when $\frac{mq_1 + nq_2}{N} \in \mathbb{N}$.

In the second part of Table I, we have shown examples of $\mathcal{Z}_2$, $\mathcal{Z}_3$, and $\mathcal{Z}_4$ to write interaction terms between the Φ_1, Φ_2 fields. For $\mathcal{Z}_2$, the charges are trivial and only cater to the possibility $q_1 = q_2 = 1, q_1 + q_2 = 2$; but for $\mathcal{Z}_3$ and $\mathcal{Z}_4$, other combinations of charges, as in Eq. (2.5), are possible. In the table, we have omitted listing the $q_1 \neq q_2, q_1 + q_2 \neq N$ case for $\mathcal{Z}_3$, as it does not exist, and for $\mathcal{Z}_4$, as it can be stabilized by kinematic constraints without any fine tuning of the couplings. All the possibilities for $\mathcal{Z}_2$ and $\mathcal{Z}_3$ symmetries to contain two DM components are discussed in this paper; for $\mathcal{Z}_2$, this turns out to be one combination, while there are six different combinations of choosing vanishingly small parameters for the case of $\mathcal{Z}_3$ to accommodate two DM components. Obviously, the number of possibilities increases with higher N. It is interesting to note that when we choose one or more couplings vanishingly small in the Lagrangian, they may indicate further restrictions or symmetries imposed to the Lagrangian.

(1) For example, when $q_1 = q_2$ and $q_1 + q_2 = N$ as in the first case as in Eq. (2.5), imposing the constraints on relevant couplings to have two DM components leads to a $\mathcal{Z}_N \otimes \mathcal{Z}'_N$ symmetric Lagrangian. This is *always* the case for $\mathcal{Z}_2$, given the only possible charge combination.

(2) On the other hand, the second and third possibilities of Eq. (2.5) eventually lead to the fourth scenario $[q_1 \neq q_2, q_1 + q_2 \neq N]$ of a higher symmetry group after assuming relevant couplings to be vanishingly small to stop heavier DS particle decay. In such

[1]However, the self-interaction terms will also be present: $\Phi_1^2, \Phi_2^2, |\Phi_1|^2, |\Phi_2|^2, \Phi_1^3, \Phi_2^3, \Phi_1|\Phi_1|^2, \Phi_2|\Phi_2|^2, \Phi_1^4, \Phi_2^4, \Phi_1^2|\Phi_1|^2, \Phi_2|\Phi_2^2|$.

[2]Additionally, for WIMP/pFIMP nature, λ_1, λ_2 can be chosen to be moderate (or small).

TABLE I. Self-interaction and interactions between two scalar fields, Φ_1 and Φ_2, which transform under a discrete symmetry $\mathcal{Z}_N$ as $\Phi_1 \to \omega_N^{q_1}\Phi_1$ and $\Phi_2 \to \omega_N^{q_2}\Phi_2$, with $\omega_N^{q_i} = e^{i2\pi(q_i/N)}$ and $q_{1,2}$ being the integer charges of $\Phi_{1,2}$ with $q_{1,2} = 1, 2, 3.., N-1$. Depending upon the choice of $q_{1,2}$, the interaction terms are shown. $\mathbb{N}$ denotes the set of integer numbers.

Two dark sector scalar fields Φ_1 and Φ_2 and interaction terms under $\mathcal{Z}_N$ symmetry		
Symmetry	Transformation	Interaction terms between DS particles
$\mathcal{Z}_N$	$\omega_N^{q_1}, \omega_N^{q_2} (q_1 = q_2)$ and $q_1 + q_2 = N$	$\Phi_1^2, \Phi_2^2, \Phi_1^4, \Phi_2^4, \Phi_1\Phi_2, \Phi_1^2\Phi_2^2, \Phi_1^3\Phi_2, \Phi_2^3\Phi_1$ $\lvert\Phi_1\rvert^2, \lvert\Phi_2\rvert^2, [\Phi_1^3, \Phi_2^3]_{\frac{3q}{N}\in\mathbb{N}}, \lvert\Phi_1\rvert^4, \lvert\Phi_2\rvert^4, \Phi_1\Phi_2^*, \lvert\Phi_1\Phi_2^*\rvert^2,$ $(\Phi_1\Phi_2^*)^2, \Phi_1\Phi_2^*(\lvert\Phi_1\rvert^2 + \lvert\Phi_2\rvert^2),$ $[\Phi_1^2\Phi_2^2, \Phi_1^3\Phi_2, \Phi_2^3\Phi_1, \Phi_1^4, \Phi_2^4]_{\frac{4q}{N}\in\mathbb{N}}, [\Phi_1^2\Phi_2, \Phi_2^2\Phi_1]_{\frac{3q}{N}\in\mathbb{N}}, [\Phi_1^3\Phi_2^*, \Phi_2^3\Phi_1^*]_{\frac{2q}{N}\in\mathbb{N}}, [\Phi_1^2\Phi_2^*, \Phi_2^2\Phi_1^*]_{\frac{q}{N}\in\mathbb{N}}$
	$\omega_N^{q_1}, \omega_N^{q_2} (q_1 = q_2 = q)$ but $q_1 + q_2 \neq N$	
	$\omega_N^{q_1}, \omega_N^{q_2} (q_1 \neq q_2)$ but $q_1 + q_2 = N$	$\lvert\Phi_1\rvert^2, \lvert\Phi_2\rvert^2, [\Phi_2^3]_{\frac{3q_2}{N}\in\mathbb{N}}, \lvert\Phi_1\rvert^4, \lvert\Phi_2\rvert^4, \Phi_1\Phi_2,$ $\Phi_1^2\Phi_2^2, \lvert\Phi_1\Phi_2\rvert^2, \Phi_1\Phi_2(\lvert\Phi_1\rvert^2 + \lvert\Phi_2\rvert^2), [\Phi_1^3, \Phi_1^2\Phi_2^*, \Phi_2^2\Phi_1^*]_{\frac{3q_1}{N}\in\mathbb{N}}, [\Phi_1^3\Phi_2^*, \Phi_2^3\Phi_1^*, \Phi_1^2\Phi_2^{*2}, \Phi_1^4, \Phi_2^4]_{\frac{4q_1}{N}\in\mathbb{N}}$
	$\omega_N^{q_1}, \omega_N^{q_2} (q_1 \neq q_2)$ and $q_1 + q_2 \neq N$	$[\Phi_1^m\Phi_2^n]_{\frac{mq_1+nq_2}{N}\in\mathbb{N}}, [\Phi_1^m\Phi_2^{*n}]_{\frac{mq_1-nq_2}{N}\in\mathbb{N}}$ where $\{m, n = 1, 2, 3$ and $q_1^{\max}, q_2^{\max} = N-1\}$
Examples of some specific symmetries: $\mathcal{Z}_2$, $\mathcal{Z}_3$, and $\mathcal{Z}_4$		
$q_1 = q_2$ and $q_1 + q_2 = N$		
$\mathcal{Z}_2$	ω_2, ω_2	$\Phi_1^2, \Phi_2^2, \Phi_1^4, \Phi_2^4, \Phi_1\Phi_2, \Phi_1^2\Phi_2^2, \Phi_1^3\Phi_2, \Phi_1\Phi_2^3$
$\mathcal{Z}_4$	ω_4^2, ω_4^2	$\Phi_1^2, \Phi_2^2, \Phi_1^4, \Phi_2^4, \Phi_1\Phi_2, \Phi_1^2\Phi_2^2, \Phi_1^3\Phi_2, \Phi_1\Phi_2^3$
$q_1 = q_2$ but $q_1 + q_2 \neq N$		
$\mathcal{Z}_3$	ω_3, ω_3 ω_3^2, ω_3^2	$\lvert\Phi_1\rvert^2, \lvert\Phi_2\rvert^2, \Phi_1^3, \Phi_2^3, \lvert\Phi_1\rvert^4, \lvert\Phi_2\rvert^4, \Phi_1\Phi_2^*, (\Phi_1\Phi_2^*)^2, \lvert\Phi_1\Phi_2\rvert^2, \Phi_1\Phi_2^2, \Phi_1^2\Phi_2, \Phi_1\Phi_2^*(\lvert\Phi_1\rvert^2 + \lvert\Phi_2\rvert^2)$
$\mathcal{Z}_4$	ω_4, ω_4 ω_4^3, ω_4^3	$\lvert\Phi_1\rvert^2, \lvert\Phi_2\rvert^2, \Phi_1^4, \Phi_2^4, \lvert\Phi_1\rvert^4, \lvert\Phi_2\rvert^4, \Phi_1\Phi_2^*, (\Phi_1\Phi_2^*)^2, (\Phi_1\Phi_2)^2, \lvert\Phi_1\Phi_2\rvert^2, \Phi_1^3\Phi_2, \Phi_2^3\Phi_1, \Phi_1\Phi_2^*(\lvert\Phi_1\rvert^2 + \lvert\Phi_2\rvert^2)$
$q_1 \neq q_2$ but $q_1 + q_2 = N$		
$\mathcal{Z}_3$	ω_3^2, ω_3 ω_3, ω_3^2	$\lvert\Phi_1\rvert^2, \lvert\Phi_2\rvert^2, \Phi_1^3, \Phi_2^3, \lvert\Phi_1\rvert^4, \lvert\Phi_2\rvert^4, \Phi_1\Phi_2, \Phi_1^2\Phi_2^2, \lvert\Phi_1\Phi_2\rvert^2, \Phi_2^2\Phi_1^*, \Phi_1^2\Phi_2^*, \Phi_1\Phi_2(\lvert\Phi_1\rvert^2 + \lvert\Phi_2\rvert^2)$
$\mathcal{Z}_4$	ω_4, ω_4^3 ω_4^3, ω_4	$\lvert\Phi_1\rvert^2, \lvert\Phi_2\rvert^2, \Phi_1^4, \Phi_2^4, \lvert\Phi_1\rvert^4, \lvert\Phi_2\rvert^4, \Phi_1\Phi_2, (\Phi_1\Phi_2)^2, (\Phi_1\Phi_2^*)^2, \lvert\Phi_1\Phi_2\rvert^2, \Phi_1^3\Phi_2^*, \Phi_2^3\Phi_1^*, \Phi_1\Phi_2(\lvert\Phi_1\rvert^2 + \Phi_2\rvert^2)$

circumstances, $\mathcal{Z}_3$ and $\mathcal{Z}_4$ symmetric cases become $\mathcal{Z}_6$ and $\mathcal{Z}_8$ symmetric scenarios, respectively. The possible charge combinations of the scalar fields pertaining to $\mathcal{Z}_3$ and $\mathcal{Z}_4$ symmetries for a single DM case and the final charge assignments under $\mathcal{Z}_6$ and $\mathcal{Z}_8$ symmetries having two DM components (after stabilization of the heavy DS particle) are listed below. We will elaborate on $\mathcal{Z}_3$ later.

$$\mathcal{Z}_3[\{q_1, q_2\}:(1,1),(2,2)] \supset \mathcal{Z}_6[\{q_1, q_2\}:(2,5),(4,1)], \tag{2.6}$$

$$\mathcal{Z}_3[\{q_1, q_2\}:(1,2),(2,1)] \supset \mathcal{Z}_6[\{q_1, q_2\}:(2,1),(4,5)], \tag{2.7}$$

$$\mathcal{Z}_4[\{q_1, q_2\}:(1,1),(3,3)] \supset \mathcal{Z}_8[\{q_1, q_2\}:(1,5),(5,1),(3,7),(7,3)], \tag{2.8}$$

$$\mathcal{Z}_4[\{q_1, q_2\}:(1,3),(3,1)] \supset \mathcal{Z}_8[\{q_1, q_2\}:(1,3),(3,1),(5,7),(7,5)]. \tag{2.9}$$

III. TWO SCALAR DM COMPONENTS UNDER SINGLE $\mathcal{Z}_2$ SYMMETRY

The $\mathcal{Z}_2$ symmetric model has been studied widely in several contexts with real scalar DM (ϕ_i), odd ($\phi_i \to -\phi_i$) under $\mathcal{Z}_2$ [69–78]. We will have a brief discussion here on the possibility of getting two DM components where two scalar fields ϕ_1 and ϕ_2 are transforming under the same $\mathcal{Z}_2$ symmetry. The corresponding Lagrangian density is

$$\mathcal{L} = \mathcal{L}_{\rm SM} + \frac{1}{2}\partial_\mu\phi_1\partial^\mu\phi_1 + \frac{1}{2}\partial_\mu\phi_2\partial^\mu\phi_2 - \mathrm{V}(\phi_1, \phi_2, \mathrm{H}), \tag{3.1}$$

where

$$\begin{aligned}\mathrm{V}(\phi_1,\phi_2,\mathrm{H}) &= \frac{1}{2}m_{\phi_1}^2\phi_1^2+\frac{1}{4!}\lambda_{\phi_1}\phi_1^4+\frac{1}{2}m_{\phi_2}^2\phi_2^2+\frac{1}{4!}\lambda_{\phi_2}\phi_2^4+\frac{1}{2}\lambda_{\phi_1\mathrm{H}}\phi_1^2\left(\mathrm{H}^\dagger\mathrm{H}-\frac{1}{2}v^2\right)\\ &+\frac{1}{2}\lambda_{\phi_2\mathrm{H}}\phi_2^2\left(\mathrm{H}^\dagger\mathrm{H}-\frac{1}{2}v^2\right)+\frac{1}{4}\lambda_{\phi_1\phi_2}\phi_1^2\phi_2^2+\frac{1}{3!}\lambda_{122}\phi_1\phi_2^3+\frac{1}{3!}\lambda_{112}\phi_1^3\phi_2\\ &+\lambda_{\phi_1\phi_2\mathrm{H}}\phi_1\phi_2\left(\mathrm{H}^\dagger\mathrm{H}-\frac{1}{2}v^2\right).\end{aligned} \tag{3.2}$$

Here, we have written the Lagrangian in physical basis where the kinetic and mass terms are diagonalized. The model parameters obey constraints from unitarity, perturbativity, and vacuum stability [35,71,79–81]. By default, the model, as in Eq. (3.2), represents a single component DM scenario, with the lighter of ϕ_1 or ϕ_2 serving as DM, where the heavier DS particle decays to DM and provides coannihilation channels for the DM to freeze out. In order to make the heavier DS particle stable, we need to analyze the interaction vertices corresponding to the possible decay channels; a detailed calculation is furnished in the Appendix B 1. Note, for example, the presence of the $\phi_1^3\phi_2$ term ($\phi_2^3\phi_1$) can lead $\phi_1(\phi_2)$ to decay into three ϕ_2 (ϕ_1). To stop this decay, one can choose a kinematical constraint like $3m_{\mathrm{DM}} > m_{\mathrm{DS}}$. However, in the presence of Higgs portal couplings, two-body decay ($\phi_2 \to h\phi_1$ or $\phi_1 \to h\phi_2$), shown in Fig. 10 (to on-shell Higgs), and three-body decays (via off-shell Higgs) are possible. Notably, for nondegenerate m_{ϕ_1,ϕ_2} masses, the decay of the heavier scalar to diphoton or digluon[3] final states via a one-loop diagram mediated by an off-shell Higgs is kinematically allowed. So, one can choose a sufficiently small portal coupling ($\lambda_{\phi_1\phi_2 H}$) so that the lifetime of the heavy scalar becomes larger than the age of the Universe. However, one-loop decay via the $\phi_1^3\phi_2$ and $\phi_2^3\phi_1$ terms is still possible; see Fig. 10. To stop them, λ_{112} and λ_{122} couplings have to be sufficiently small as well; see Table VI for the order of magnitude.

Interestingly, when we block these couplings to stabilize the heavier DS particle, we essentially get rid of all terms having combinations of $\phi_1\phi_2$, and then, the Lagrangian eventually reduces to a $\mathcal{Z}_2 \otimes \mathcal{Z}_2'$ symmetric one well studied in different contexts, like in the WIMP-WIMP scenario [35], WIMP-pFIMP scenario [42], etc. The only subtle difference between a pure $\mathcal{Z}_2 \otimes \mathcal{Z}_2'$ symmetric scenario and that of a single $\mathcal{Z}_2$ with two DM components is that, for the latter, we are getting one stable DM and one LLP, while under a two different $\mathcal{Z}_2$ symmetry, we get two stable DM components, although the phenomenology is identical in both cases.

IV. TWO SCALAR DM COMPONENTS UNDER SINGLE $\mathcal{Z}_3$ SYMMETRY

In this section, we will discuss two complex scalar fields transforming under single $\mathcal{Z}_3$ symmetry and its phenomenology in single and two-component DM scenarios. We will also discuss the comparison with the two-component DM scenario in the $\mathcal{Z}_3 \otimes \mathcal{Z}_3'$ setup [82].

A. Model

The SM extended dark sector Lagrangian containing two complex scalar fields that transform differently under $\mathcal{Z}_3$ symmetry (see Table II) is written as [67,82–88]

$$\mathcal{L} = \mathcal{L}_{\mathrm{SM}} + |\partial_\mu\chi_1|^2 + |\partial_\mu\chi_2|^2 - V(\chi_1,\chi_2,\mathrm{H}), \tag{4.1}$$

where

$$\begin{aligned}V(\chi_1,\chi_2,\mathrm{H}) &= \sum_{i=1,2}\left(m_{\chi_i}^2|\chi_i|^2+\lambda_{\chi_i}|\chi_i|^4+\lambda_{iH}|\chi_i|^2\left(\mathrm{H}^\dagger H-\frac{v^2}{2}\right)\right)\\ &+\lambda_{12}|\chi_1|^2|\chi_2|^2+\frac{1}{2}\lambda_{12H}(\chi_1\chi_2+\mathrm{H.c.})\left(\mathrm{H}^\dagger H-\frac{v^2}{2}\right)+\frac{1}{2}\lambda'_{12}(\chi_1^2\chi_2^2+\mathrm{H.c.})\\ &+\frac{1}{2}[\mu_1\chi_1^*\chi_2^2+\mu_2\chi_1^2\chi_2^*+\mu_3\chi_1^3+\mu_4\chi_2^3+\mathrm{H.c.}]\\ &+\frac{1}{2}[\lambda_3\chi_1\chi_2|\chi_1|^2+\lambda_4\chi_1\chi_2|\chi_2|^2+\mathrm{H.c.}].\end{aligned} \tag{4.2}$$

[3]However, two gluons eventually form bound states that are not massless. In that case, they will be subjected to the specific phase space constraints' availability.

TABLE II. Model particle contents and their transformation with $\omega = e^{i2\pi/3}$.

DS fields	$\mathcal{Z}_3$
Complex scalar χ_1	ω/ω^2
Complex scalar χ_2	ω^2/ω

In Eq. (4.1), we may have the kinetic mixing terms and mass mixing terms, which can be removed through an appropriate field rotation and redefinition, as discussed in detail in the Appendix A. Here, we assume that Eq. (4.2) is written in the physical basis obtained after two successive rotations in which the kinetic and mass mixing matrices are diagonalized. We must also emphasize that the diagonalization does not alter the interaction terms. For $\lambda_H, \lambda_i > 0$ and $\mu_H^2 < 0$, the Higgs field acquires nonzero vacuum expectation value (VEV) (v), with $\mathrm{H} = (0\ (h+v)/\sqrt{2})^{\mathrm{T}}$, and results in electroweak symmetry breaking. Here, we do not assume any VEV for the complex fields, and all couplings in the scalar potential are taken to be real in order to ensure Charge-Parity (CP) invariance. The theoretical and experimental constraints on the model parameters are as follows.

1. Unitarity

The unitarity bounds, derived in the infinite scattering energy limit and considering only the quartic terms, are given by [85,89,90]

$$|\lambda_H| \leq 4\pi, \qquad |\lambda_{12} - 2\lambda'_{12}| \leq 8\pi, \tag{4.3}$$

$$|\lambda_{1H} + \lambda_{2H} \pm \sqrt{(\lambda_{1H} - \lambda_{2H})^2 + \lambda_{12H}^2}| \leq 16\pi, \tag{4.4}$$

while for the others, please see Appendix C.

2. Perturbativity

To ensure the validity of perturbation theory, loop corrections to the couplings should be smaller than their tree-level values. The perturbative bound for the model is given by [91]

$$|\lambda_{iH}| \leq 4\pi, \qquad |\lambda_i| < \pi. \tag{4.5}$$

3. Vacuum stability

The necessary conditions required to stabilize the potential are

$$\lambda_H > 0, \qquad \lambda_i > 0, \qquad \lambda_{iH} + 2\sqrt{\lambda_i \lambda_H} > 0. \tag{4.6}$$

The maximal allowed value of the cubic parameters $\mu_{3,4}$ is approximately equal to $\mu_3 = 2\sqrt{\lambda_{\chi_1}} m_{\chi_1}$, $\mu_4 = 2\sqrt{\lambda_{\chi_2}} m_{\chi_2}$ [85,92–94]. However, we take the cubic coupling up to twice the lightest DM mass for simplicity.

4. Higgs invisible decay width

The search for invisible decays with the ATLAS detector [95], using 139 fb^{-1} of proton-proton collision data at a center-of-mass energy of $\sqrt{s} = 13$ TeV at the LHC, combined with results obtained at $\sqrt{s} = 7$ TeV and $\sqrt{s} = 8$ TeV, sets an observed (expected) upper limit of 0.107(0.077) on the Higgs boson branching ratio to invisible final states at the 95% confidence level. A combined analysis of $\sqrt{s} = 7$, 8, and 13 TeV proton-proton collision data at the CMS detector [96] sets an observed (expected) 95% confidence level upper limit of 0.15(0.08) on $\mathcal{B}(h \to \mathrm{inv})$.

B. Single component DM

In the potential given by Eq. (4.2), we have written all possible terms respecting the $\mathcal{Z}_3$ symmetry. Note that the term $\chi_1\chi_2$ can be written since both χ_1 and χ_2 rotate under the same $\mathcal{Z}_3$, which is not present in $\mathcal{Z}_3 \otimes \mathcal{Z}'_3$ [82]. But the presence of this term gives us a nondiagonal mass term unless we choose $\mu_{12}^2 = -\lambda_{12H} v^2/2$.

By default, the Lagrangian describes a complex scalar singlet DM, stable under $\mathcal{Z}_3$ symmetry, which has been studied in different contexts [86,97]. Here, we recap this scenario with the trending bounds on DM available from direct and indirect searches. Here, we have taken χ_1 as our DM, but χ_2 is equally possible, and DM phenomenology remains unaltered. The relic density of DM is governed by its annihilation channels. Additionally, we can have coannihilation and semiannihilation contribution in the presence of heavy DS particles. This new degree of freedom gives more allowed parameter space compared to the only one $\mathcal{Z}_3$ symmetric DM scenario [83,85]. As we focus on GeV scale DM, $n \to 2$ ($n > 2$) depletion processes are always subdominant to the $2 \to 2$ annihilation process. The heavy DS particle decays to DM via off-shell or on-shell Higgs in tree or loop level due to sizable portal couplings $(\lambda_{12H}, \lambda_3, \mu_2)$. The key free parameters that govern DM analysis are

$$\{m_{\chi_i}, \lambda_j, \mu_j, \lambda_{iH}, \lambda_{12H}, \lambda_{12}, \lambda'_{12}\}, \tag{4.7}$$

where $i = 1, 2$ and $j = 1, \ldots, 4$, and all of these are taken as real parameters. Mass kinematics and couplings are the key parameters for the heavier DS decay to DM and to get only one stable DM.

1. BEQ and relic density

The Boltzmann equation (BEQ) in this case is relevant to the total yield, $Y_\chi = \sum_i Y_i = Y_{\chi_1} + Y_{\chi_1^*} + Y_{\chi_2} + Y_{\chi_2^*}$, including the complex conjugate fields and heavier dark sector fields as the heavier ones decay to DM, and IT is given by [43,63,64,66,82,98]

$$\frac{dY_\chi}{dx} = -\frac{s}{xH(x)}\left[\langle\sigma v\rangle^{\rm eff}_{\rm SM}(Y_\chi^2 - Y_\chi^{eq^2}) + \frac{1}{2}\langle\sigma v\rangle^{\rm eff}_{\rm semi}(Y_\chi^2 - Y_\chi Y_\chi^{eq})\right], \tag{4.8}$$

where

$$\langle\sigma v\rangle^{\rm eff}_{\rm SM} = \sum_{i,j}\langle\sigma v\rangle_{ij\to {\rm SM\,SM}}\frac{n_i^{\rm eq} n_j^{\rm eq}}{(n_\chi^{\rm eq})^2},$$
$$\langle\sigma v\rangle^{\rm eff}_{\rm semi} = \sum_{i,j,k}\langle\sigma v\rangle_{ij\to k\ {\rm SM}}\frac{n_i^{\rm eq} n_j^{\rm eq}}{(n_\chi^{\rm eq})^2}$$

and

$$n_\chi^{\rm eq} = \sum_i n_i^{\rm eq} = n_{\chi_1}^{eq} + n_{\chi_1^*}^{eq} + n_{\chi_2}^{eq} + n_{\chi_2^*}^{eq}.$$

We can also express the effective semiannihilation cross section as

$$\langle\sigma v\rangle^{\rm eff}_{\rm SM} = \left[\sum_i g_i m_i^2 K_2\left(\frac{m_i}{T}\right)\right]^{-2}\sum_{i,j}\langle\sigma v\rangle_{ij\to {\rm SM\,SM}} g_i g_j m_i^2 m_j^2 \times K_2\left(\frac{m_i}{T}\right)K_2\left(\frac{m_j}{T}\right), \tag{4.9}$$

where g_i denotes internal degrees of freedom and K_2 denotes a Bessel function of the second kind. We have numerically solved the BEQ, Eq. (4.8), and verified it using MICROMEGAS [99] after importing the $\mathcal{Z}_3$ symmetric model using FeynRules [100]. The solutions of the BEQ and relic density-allowed parameter space in terms of relevant parameters as well as direct and indirect search constraints are shown in Fig. 1.

In Fig. 1(a), we show the relic under abundance in terms of DM mass and Ωh^2. The rainbow color bar shows the variation in λ_{1H}. With the presence of Higgs-mediated s-channel diagrams, Higgs resonance drop is observed at $m_{\chi_1} \sim m_h/2$. The presence of a semiannihilation process, $\chi_i\chi_j \to \chi_k h$, provides another dip near $m_{\chi_1} \sim m_h$. DM relic density decreases with larger portal and cubic couplings through annihilation, coannihilation, and semiannihilation. When we move away from the Higgs mass regime, the relic density decreases due to less (semi)annihilation contribution and requires larger λ_{1H} coupling. The shape of the parameter space is otherwise very typical of a single component scalar DM model connected via Higgs portal. The semiannihilation and coannihilation contribution moves the whole spectrum downward toward smaller relic density and allows smaller values of λ_{1H}.

2. Direct detection limit from WIMP-nucleon inelastic scattering

The relic density-allowed parameter space is further constrained by nonobservation of DM in direct search, resulting in a lower bound on the DM-nucleon scattering cross section from direct detection experiments like XENONnT [45] and LUX-ZEPLIN [46]. The self-annihilation and semiannihilation of this $\mathcal{Z}_3$ WIMP are also constrained by the *Fermi*-LAT [48], CTA [55], and H.E.S.S. [51] data.

The DM-nucleon scattering is governed mainly by the Higgs portal interaction term $\chi_1\chi_1^*(H^\dagger H)$. For complex scalar DM, the spin-independent DM-nucleon inelastic scattering cross section is an observed quantity in direct detection experiments,

$$\sigma^{\rm SI}_{\chi_1} = \frac{\mu_n^2 m_n^2}{4\pi v^2 m_{\chi_1}^2}\frac{f_n^2}{m_h^4}\lambda^2_{h\chi_1\chi_1^*}, \tag{4.10}$$

where $\mu_n = \frac{m_n m_{\chi_1}}{m_n + m_{\chi_1}}$, $\lambda_{h\chi_1\chi_1^*} = \lambda_{1H} v$, and other parameters have the usual meaning. Equation (4.10) shows that the spin-independent scattering cross section depends on the DM mass (m_{χ_1}) and Higgs portal coupling (λ_{1H}). So, to satisfy direct search bound, we wish to decrease λ_{1H} and adjust other parameters to satisfy relic density, where coannihilation and semiannihilation play a major role.

In Fig. 1(b), we have shown the relic density-allowed parameter space in the $m_{\chi_1} - \sigma^{\rm SI}_{\chi_1}$ plane, and the color bar represents the mass splitting between χ_1 and χ_2, which characterizes the coannihilation contribution to relic density. Parameters kept fixed are mentioned in the figure inset.

We see that no relic density-allowed points are seen at the resonance region or in the semiannihilation region; they correspond to an underabundant region. This is simply due to the range of λ_{1H} chosen for the scan, as it requires much smaller values to satisfy relic, due to enhancement in the effective annihilation cross section in these regions. If the DM mass is adequately large and away from the Higgs mass region, then semiannihilation is small, and we need smaller Δm, which enhances coannihilation. In Fig. 1(b), some region of the parameter space above the Higgs mass regime is excluded by the recent XENONnT and LZ-2022 bounds, represented by light blue and olive green lines, respectively. The three dashed lines correspond to the projected limit spin-independent DM direct detection cross section. The parameter space illustrated here is particular for this benchmark, and one can get more relic density-allowed regions depending on the values of the parameters kept fixed.

3. Indirect detection limit on the self-annihilation of WIMPs

The limits on DM self-annihilation impose another constraint on the relic- and DD-allowed parameter space of the model. Here, we are using the indirect search limit on

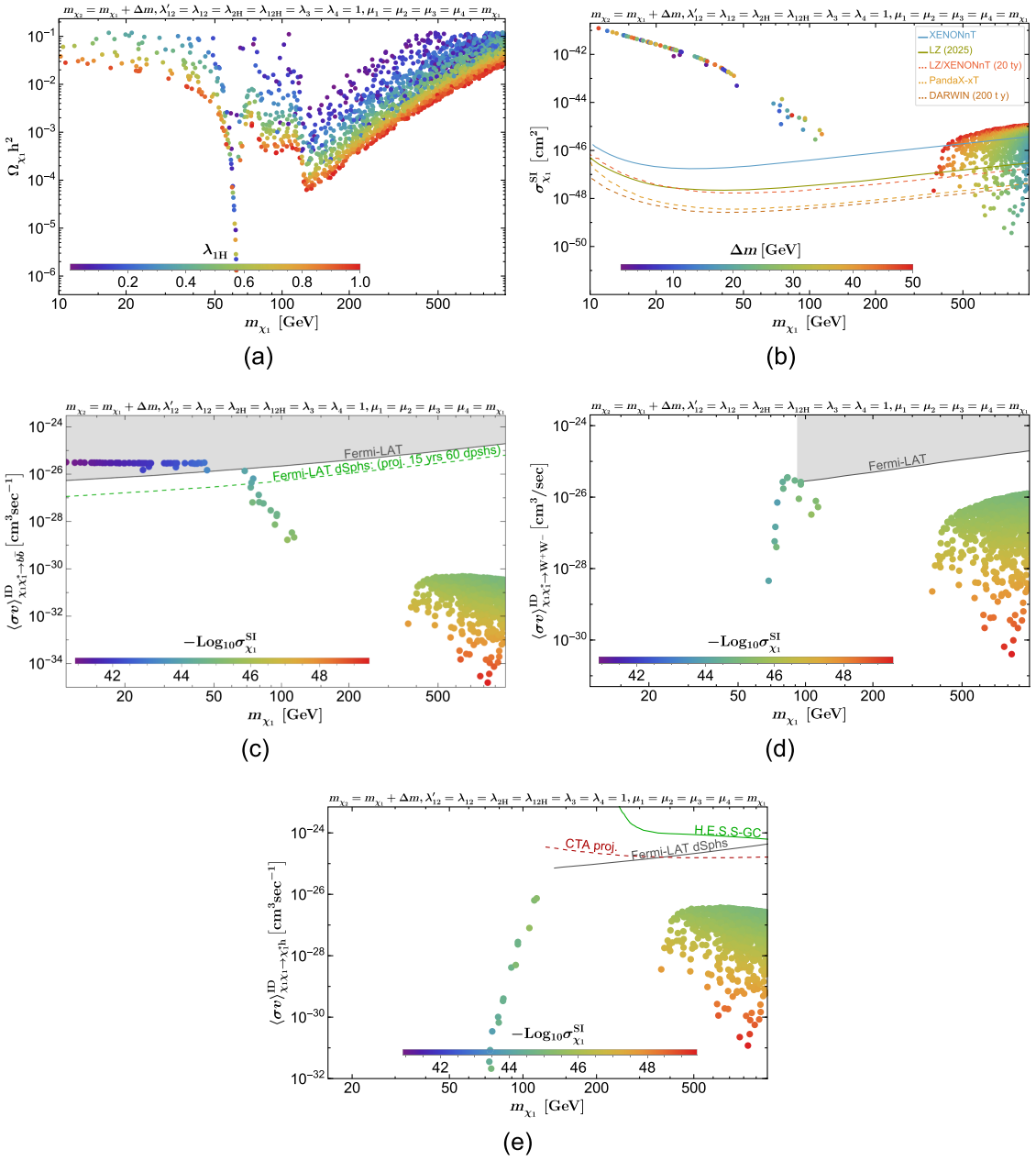


FIG. 1. Relic density-allowed parameter space of the single component DM model with two scalars transforming under the same $\mathcal{Z}_3$ symmetry, confronting direct and indirect search limits. Panel (a) shows relic under abundant ($\Omega_{\chi_1}h^2 \leq 0.1212$) parameter space in the $m_{\chi_1} - \Omega_{\chi_1}h^2$ plane; the rainbow color bar shows the variation in the Higgs portal coupling (λ_{1H}) with DM (χ_1) mass. Panel (b) shows relic-allowed parameter space in the $m_{\chi_1} - \sigma^{\rm SI}_{\chi_1}$ plane, and the rainbow color bar here shows DM mass splitting with the coannihilating partner χ_2, i.e, $\Delta m = m_{\chi_2} - m_{\chi_1}$. The light blue and olive green colored lines represent the XENONnT and LZ-2022 bounds. Panels (c), (d) show the relic density-allowed parameter space in the $m_{\chi_1} - \langle\sigma v\rangle_{\chi_1\chi_1^*\to b\bar{b}(W^+W^-)}$ plane, and the rainbow color bar shows the variation in $\sigma^{\rm SI}_{\chi_1}$ in units of cm^2. Thick gray and dashed green lines portray the *Fermi*-LAT observation and projected limit [48,49,101], respectively. Panel (e) shows the relic density-allowed region in the $m_{\chi_1} - \langle\sigma v\rangle_{\chi_1\chi_1\to\chi_1^* h}$ plane, and the rainbow color bar represents the spin-independent inelastic scattering cross section ($\sigma^{\rm SI}_{\chi_1}$) variation. The thick green, thick gray, and dashed blue lines represent the upper bound of the DM semiannihilation from H.E.S.S, *Fermi*-LAT, and CTA, respectively.

DM self-annihilation from the *Fermi* collaboration, 6 years of observation using 15 dwarf spheroidal galaxies (dSphs) [48], and a projected sensitivity for 45 dSphs and 15 years of observation [49]. The thick gray and dashed green lines in Fig. 1(c) represent the observed and projected limit from *Fermi*-LAT [48]. At the same time, the gray-shaded region is excluded by the observed *Fermi*-LAT limit on DM self-annihilation into bottom pairs.

The indirect detection limit on the thermal average DM (χ_1) self-annihilation to the bottom pair is evaluated at the DM freeze-out point, $T^{FO}_{\chi_1} \sim m_{\chi_1}/25$, which depends on the DM mass (m_{χ_1}) and Higgs portal coupling (λ_{1H}). The thermal average cross section, $\langle\sigma v\rangle_{\chi_1\chi_1^*\to b\bar{b}}$, is nearly constant below the $m_h/2$ region but maximum near the Higgs resonance. Near the Higgs mass, semiannihilation helps decrease the λ_{1H} coupling. The DM mass region, near and below the Higgs resonance, is mostly excluded for the specific choice of the benchmark point and allowed above the resonance region. To see the corresponding DD cross section, see the rainbow color bar in Fig. 1(c).

4. Indirect detection limit on the semiannihilation of WIMPs

Recently, the gamma-ray observations from *Fermi*-LAT [48], the H.E.S.S [51] telescope, and CTA [55] provide a conservative projected limit on the DM (χ_1) semiannihilation. The presence of cubic interaction in $\mathcal{Z}_3$ symmetric WIMPs provides a semiannihilation channel via $\langle\sigma v\rangle_{\chi_1\chi_1\to\chi_1^* h}$ and is evaluated at the freeze-out point of χ_1 having an s-wave contribution of $\chi_1\chi_1^* \to \chi_1 h$. This cross section depends on $m_{\chi_1}, m_{\chi_2}, \lambda_{1H}, \lambda_{12H}, \mu_2$, and μ_3. In Fig. 1(e), we show the relic density-allowed parameter space $m_{\chi_1} - \langle\sigma v\rangle^{\rm ID}_{\chi_1\chi_1\to\chi_1^* h}$ plane. The color bar shows variation with respect to the DD cross section. We see that for the chosen values of the parameters, relic density-allowed points lie below the existing limits. Like the other plots, the absence of points near the Higgs resonance and the Higgs mass can be seen, mainly due to the range of parameters chosen for the scan. However, the DM is well allowed up to TeV due to coannihilation and self-annihilation processes through the presence of additional complex scalar χ_2 transforming under the same symmetry [83].

C. Two-component DM

Equation (4.1) describes the extension of the SM containing two complex scalar fields that transform differently under a single $\mathcal{Z}_3$ symmetry with the charge combinations of the fields $q_1 \neq q_2$ and $q_1 + q_2 = N$. Interaction terms depend on their transformation charges; see Table III for details. For the charge combinations $q_1 = q_2$ and $q_1 + q_2 \neq N$, the interaction terms can be found in Table IV. Such interaction terms between χ_1 and χ_2, like $\chi_1^2\chi_2^*$, $\chi_2^2\chi_1^*$, etc., open up the decay of the heavier component to the lighter one(s). A suitable choice of mass hierarchy, $2m_{\rm lighter} > m_{\rm higher}$, can stop such decay. Further, both fields are connected with the visible sector via Higgs portal interactions. The one connecting both the fields, like $\chi_1\chi_2|H|^2$, leads to the decay of the heavier component to the lighter one plus the SM at tree level. A mass hierarchy like $m_{\chi_2} > m_{\chi_1} + m_h$ can stop such on-shell decay; however, off-shell Higgs decay to diphoton or digluon is always permitted for nondegenerate masses of the dark sector particles. A sufficiently small portal coupling (λ_{12H}) associated with this term can stop on-shell or off-shell decay of the heavier particle to SM at tree level. However, one-loop and two-loop decay terms are still possible in the presence of self-interaction terms between χ_1 and χ_2. Hence, even after neglecting λ_{12H}, one needs to choose very small λ_3, λ_4, and μ_2 to restrict one-loop decay, although the choice of μ_2 is not unique. However, after sacrificing all of these parameters, the two-loop decay (see Appendix B 2) is still possible. To restrict the two-loop decay, different parameters can be chosen to be small, giving rise to different kinds of scenarios, as shown in Table III. The boldface terms in Table III can be sacrificed to obtain the second long lived DM component. In Table VII in the Appendix B 2, we have also given an estimate of the smallness of these couplings, $\lambda_3, \lambda_4, \lambda_{12H}, \mu_2 \lesssim 10^{-15}$, so that the decay lifetime is larger than the age of the Universe. Note that for the $\mathcal{Z}_3$ model, the possibility of $q_1 \neq q_2, q_1 + q_2 \neq N$ does not arise. Therefore, one has to sacrifice some couplings to make both components stable. We also provide, for reference, the terms that are absent in the $q_1 = q_2$ scenario (Table IV) (marked in boldface), although we will not analyse this case in detail.

Depending on the choice of the couplings required to stabilize the heavier DM component, six possibilities emerge, as shown in Table III ($q_1 \neq q_2$) and Table IV ($q_1 = q_2$). The absence of boldface terms indicates the

TABLE III. Terms having two dark sector scalar fields oppositely transforming under discrete symmetry $\mathcal{Z}_3$. The boldface terms are the minimum number of terms to be sacrificed to stop the tree- and loop-level decays of the heavier DS particle.

Scenarios	Interaction terms of two DM components: χ_1 and χ_2 under $\mathcal{Z}_3$ symmetry
	$q_1 = 1, q_2 = 2$ or $q_1 = 2, q_2 = 1$
A	$\lvert\chi_1\rvert^2 H^\dagger H, \lvert\chi_2\rvert^2 H^\dagger H, \chi_1^3, \chi_2^3, \lvert\chi_1\rvert^4, \lvert\chi_2\rvert^4, \boldsymbol{\chi_1\chi_2 H^\dagger H}, \boldsymbol{\chi_1^2\chi_2^2}, \lvert\chi_1\chi_2\rvert^2, \boldsymbol{\chi_2^2\chi_1^*}, \boldsymbol{\chi_1^2\chi_2^*}, \boldsymbol{\chi_1\chi_2}(\lvert\boldsymbol{\chi_1}\rvert^2 + \lvert\boldsymbol{\chi_2}\rvert^2)$
B	$\lvert\chi_1\rvert^2 H^\dagger H, \lvert\chi_2\rvert^2 H^\dagger H, \chi_1^3, \boldsymbol{\chi_2^3}, \lvert\chi_1\rvert^4, \lvert\chi_2\rvert^4, \boldsymbol{\chi_1\chi_2 H^\dagger H}, \chi_1^2\chi_2^2, \lvert\chi_1\chi_2\rvert^2, \chi_2^2\chi_1^*, \boldsymbol{\chi_1^2\chi_2^*}, \boldsymbol{\chi_1\chi_2}(\lvert\boldsymbol{\chi_1}\rvert^2 + \lvert\boldsymbol{\chi_2}\rvert^2)$
C	$\lvert\chi_1\rvert^2 H^\dagger H, \lvert\chi_2\rvert^2 H^\dagger H, \boldsymbol{\chi_1^3}, \chi_2^3, \lvert\chi_1\rvert^4, \lvert\chi_2\rvert^4, \boldsymbol{\chi_1\chi_2 H^\dagger H}, \chi_1^2\chi_2^2, \lvert\chi_1\chi_2\rvert^2, \boldsymbol{\chi_2^2\chi_1^*}, \chi_1^2\chi_2^*, \boldsymbol{\chi_1\chi_2}(\lvert\boldsymbol{\chi_1}\rvert^2 + \lvert\boldsymbol{\chi_2}\rvert^2)$

TABLE IV. Interaction terms between two DS scalar fields, χ_1 and χ_2, carrying identical $\mathcal{Z}_3$ charges. The highlighted boldface terms represent the minimal set that must be eliminated to prevent both tree-level and loop-level decays of the heavier DS particle.

Scenarios	Interaction terms of two DM components: χ_1 and χ_2 under $\mathcal{Z}_3$ symmetry
	$q_1 = q_2 = 1, 2$
D	$\lvert\chi_1\rvert^2\mathrm{H}^\dagger\mathrm{H}, \lvert\chi_2\rvert^2\mathrm{H}^\dagger\mathrm{H}, \chi_1^3, \chi_2^3, \lvert\chi_1\rvert^4, \lvert\chi_2\rvert^4, \boldsymbol{\chi_1\chi_2^*\mathrm{H}^\dagger\mathrm{H}}, \boldsymbol{(\chi_1\chi_2^*)^2}, \lvert\chi_1\chi_2\rvert^2, \boldsymbol{\chi_2^2\chi_1}, \boldsymbol{\chi_1^2\chi_2}, \boldsymbol{\chi_1\chi_2^*}(\lvert\boldsymbol{\chi_1}\rvert^2 + \lvert\boldsymbol{\chi_2}\rvert^2)$
E	$\lvert\chi_1\rvert^2\mathrm{H}^\dagger\mathrm{H}, \lvert\chi_2\rvert^2\mathrm{H}^\dagger\mathrm{H}, \chi_1^3, \boldsymbol{\chi_2^3}, \lvert\chi_1\rvert^4, \lvert\chi_2\rvert^4, \boldsymbol{\chi_1\chi_2^*\mathrm{H}^\dagger\mathrm{H}}, (\chi_1\chi_2^*)^2, \lvert\chi_1\chi_2\rvert^2, \chi_2^2\chi_1, \boldsymbol{\chi_1^2\chi_2}, \boldsymbol{\chi_1\chi_2^*}(\lvert\boldsymbol{\chi_1}\rvert^2 + \lvert\boldsymbol{\chi_2}\rvert^2)$
F	$\lvert\chi_1\rvert^2\mathrm{H}^\dagger\mathrm{H}, \lvert\chi_2\rvert^2\mathrm{H}^\dagger\mathrm{H}, \boldsymbol{\chi_1^3}, \chi_2^3, \lvert\chi_1\rvert^4, \lvert\chi_2\rvert^4, \boldsymbol{\chi_1\chi_2^*\mathrm{H}^\dagger\mathrm{H}}, (\chi_1\chi_2^*)^2, \lvert\chi_1\chi_2\rvert^2, \boldsymbol{\chi_2^2\chi_1}, \chi_1^2\chi_2, \boldsymbol{\chi_1\chi_2^*}(\lvert\boldsymbol{\chi_1}\rvert^2 + \lvert\boldsymbol{\chi_2}\rvert^2)$

presence of a new discrete symmetry, as mentioned before. For example, scenarios A and D correspond to the $\mathcal{Z}_3 \otimes \mathcal{Z}_3'$ scenario. Similarly, scenarios B and C turn out to be $\mathcal{Z}_6$ symmetry with $q_1 = 4$, $q_2 = 5$ or $q_1 = 2$, $q_2 = 1$ and $q_1 = 5$, $q_2 = 4$ or $q_1 = 1$, $q_2 = 2$, respectively. Scenarios E and F fall under $\mathcal{Z}_6$ with $q_1 = 4$, $q_2 = 1$ or $q_1 = 2$, $q_2 = 5$ and $q_1 = 1$, $q_2 = 4$ or $q_1 = 5$, $q_2 = 2$, respectively. These observations are summarized in Table V. Let us recall that when we can have $q_1 \neq q_2, q_1 + q_2 \neq N$, we can stabilize both the components kinematically.

Further, if we want one of the components to be pFIMPs, we have to choose the corresponding portal coupling feeble but DM-DM interaction sizable. Now the scenarios that arise here, having two DM components, are not all independent. In the following, we elaborate upon scenarios A and B; scenarios C, D, E, and F are somewhat similar to them.

1. Scenario A

From Table III, we see that this particular scenario arises via tiny couplings associated with $\chi_1\chi_2\mathrm{H}^\dagger H, \chi_1^2\chi_2^2, \chi_2^2\chi_1^*, \chi_1^2\chi_2^*, \chi_1\chi_2\lvert\chi_1\rvert^2, \chi_1\chi_2\lvert\chi_2\rvert^2$ interaction terms to give rise to one LLP and one stable DM. This is then equivalent to the $\mathcal{Z}_3 \otimes \mathcal{Z}_3'$ scenario [82]. But, in the two WIMP case, limited parameter space is left for future direct detection. However, the WIMP-pFIMP possibility enhances the allowed parameter space, as discussed below.

TABLE V. The resultant symmetries after imposing stabilization conditions on DS particles from the $\mathcal{Z}_3$ symmetric Lagrangian.

DS particles and charges		DM particles symmetry and charges		
Symmetry and charges	Scenarios	Resulting symmetry	q_1	q_2
$\mathcal{Z}_3$: (q_1, q_2) $= (1, 2)$ or $(2, 1)$	A	$\mathcal{Z}_3 \otimes \mathcal{Z}_3'$	1	1, 2
			2	1, 2
	B	$\mathcal{Z}_6$	4	5
			2	1
	C	$\mathcal{Z}_6$	5	4
			1	2
$\mathcal{Z}_3$: (q_1, q_2) $= (1, 1)$ or $(2,2)$	D	$\mathcal{Z}_3 \otimes \mathcal{Z}_3'$	1	1, 2
			2	1, 2
	E	$\mathcal{Z}_6$	4	1
			2	5
	F	$\mathcal{Z}_6$	1	4
			5	2

To make the LLP (χ_2) pFIMP, we further need λ_{2H} to be very tiny; see Appendix B 2 to know the range of couplings. Then, the available parameters that could be utilized in WIMP-pFIMP phenomenology are

$$\{m_{\chi_1}, m_{\chi_2}, \lambda_{\chi_1}, \lambda_{\chi_2}, \lambda_{1H}, \lambda_{12}, \mu_3, \text{ and } \mu_4\}. \tag{4.11}$$

2. Relic density

The total relic abundance for this WIMP-pFIMP setup comes from χ_1 as WIMP and χ_2 as pFIMP to stipulate to

$$\Omega_{\mathrm{DM}}\mathrm{h}^2 = 2.744 \times 10^8 \sum_{i=1,2} m_{\chi_i} Y_i[x_\infty], \tag{4.12}$$

where $Y_i = n_i/s$, n_i is the number density and s is the entropy density. The DM yield (Y_i) is calculated by solving coupled BEQ for χ_1 and χ_2 numerically using MICROMEGAS. The self-annihilation, semiannihilation, conversion, and semiconversion are the main number-changing processes that contribute to the DM relic. It is worth recalling that after stabilization of the heavy component, there is no coannihilation contribution.

3. Direct detection limits on WIMPs and pFIMPs

The WIMP is weakly coupled to the visible sector via the Higgs portal interaction and can scatter with the detector nucleon. The effective WIMP-nucleon inelastic scattering cross section at zero transfer momentum limit ($q_h^2 = t \to 0$) turns out to be [see Fig. 2(a)]

$$\sigma_{\chi_1}^{\mathrm{eff}} = \frac{\Omega_{\chi_1} h^2}{\Omega_{\chi_1} h^2 + \Omega_{\chi_2} h^2} \frac{\mu_n^2 m_n^2}{4\pi v^2 m_{\chi_1}^2} \frac{f_n^2}{m_h^4} \lvert\lambda_{h\chi_1\chi_1^*}\rvert^2. \tag{4.13}$$

In the above, $\mu_n = \frac{m_n m_{\chi_1}}{m_n + m_{\chi_1}}$, where m_n is the nucleon mass, $f_n = \frac{2}{9} + \frac{7}{9}\sum_{u,d,s} f_{T_q}^n$ with $f_{T_u}^{p(n)} = 0.018(0.013)$, $f_{T_d}^{p(n)} = 0.027(0.040)$, and $f_{T_s}^{p(n)} = 0.037(0.037)$ [102].

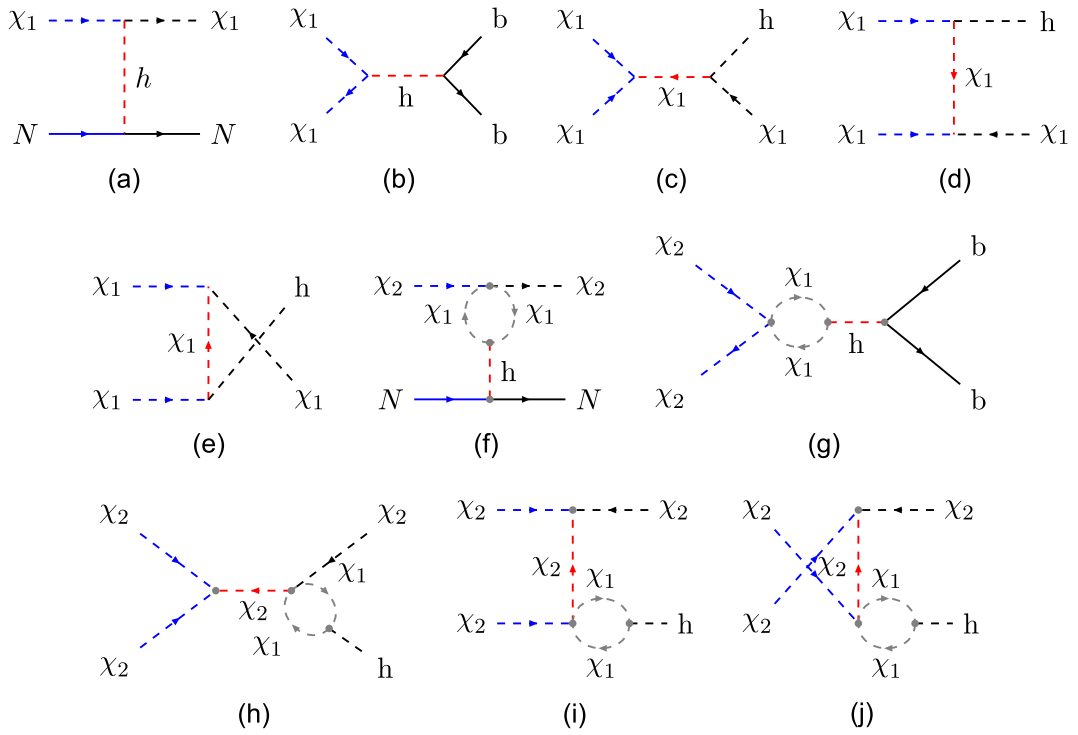


FIG. 2. Top: Panels (a) and (b) represent Feynman diagrams corresponding to the direct and indirect detection of WIMPs (χ_1), respectively. Panels (c)–(e) correspond to WIMP semiannihilation processes, contributing to the indirect search. Bottom: Panel (f) shows pFIMP direct search, and panels (g)–(j) represent processes that contribute to indirect detection of pFIMPs (χ_2).

The direct detection of pFIMPs is possible only by the WIMP loop-mediated penguin and vertex correction diagrams; see Fig. 2(f). The effective spin-independent pFIMP-nucleon ($\chi_2 - N$) inelastic scattering cross section at zero transfer momentum ($q_h^2 = t \to 0$) limit is given by

$$\sigma_{\chi_2}^{\rm eff} = \frac{\Omega_{\chi_2} h^2}{\Omega_{\chi_1} h^2 + \Omega_{\chi_2} h^2} \frac{\mu_n^2 m_n^2}{4\pi v^2 m_{\chi_2}^2} \frac{f_n^2}{m_h^4} |\Gamma^{\rm total}_{h\chi_2\chi_2^*}|^2_{t\to 0}, \quad (4.14)$$

where $\mu_n = \frac{m_n m_{\chi_2}}{m_n + m_{\chi_2}}$ and $\Gamma^{\rm total}_{h\chi_2\chi_2^*} = \Gamma^{2f}_{h\chi_2\chi_2^*}$. One can easily calculate

$$\Gamma^{2f}_{h\chi_2\chi_2^*}(q_h^2) = -i\lambda^{\rm relic}_{h\chi_2\chi_2^*} - i\frac{\lambda_{\chi_1\chi_1^*\chi_2\chi_2^*}\lambda_{h\chi_1\chi_1^*}}{16\pi^2} \times \int_0^1 dx \, \ln\left[\frac{m_{\chi_1}^2 - x(1-x)4m_{\chi_2}^2}{m_{\chi_1}^2 - x(1-x)q_h^2}\right], \quad (4.15)$$

where q_h is the transfer momentum associated with Higgs, $\lambda_{\chi_1\chi_1^*\chi_2\chi_2^*} = -i\lambda_{12}$, and $\lambda_{h\chi_1\chi_1^*} = -i\lambda_{1H}v$. Using Eqs. (4.13) and (4.14), we impose the presently available direct detection constraint from LUX-ZEPLIN, XENONnT, and PandaX-xT experiments on the relic density-allowed parameter space of the model. Figures 3(a) and 3(b) show the relic density-allowed parameter space in the $m_{\chi_1} - \sigma_{\chi_1}^{\rm eff}$ plane (corresponding to WIMPs) while the rainbow color bar represents the DM mass difference and λ_{1H}, respectively. Here, we have taken $\mu_3 = 2m_{\chi_1}$ and $\mu_4 = 2m_{\chi_2}$, which are the most useful parameters for DM semiannihilation. The Higgs resonance ($m_{\chi_1} \sim m_h/2$) and semiannihilation ($m_{\chi_1} \sim m_h$) of the WIMP help it to acquire underabundance, while the total relic is adjusted by the pFIMP, and we relax the λ_{1H} to come under the present DD bound. Beyond the Higgs resonance or semiannihilation regime, the cross section decreases and relic density increases, which is adjusted by enhancing the portal coupling λ_{1H}, respecting the DD bound.

Figures 3(c) and 3(d) represent DM relic density-allowed parameter space in the $m_{\chi_2} - \sigma_{\chi_2}^{\rm eff}$ plane corresponding to pFIMPs. The spin-independent scattering cross section $\sigma_{\chi_2}^{\rm eff}$ depends on the total loop amplitude ($\Gamma^{\rm total}_{h\chi_2\chi_2^*}$), which is a function of $\lambda_{12}, \lambda_{1H}$, and μ_1 couplings, and they decide which process in Fig. 2(f) dominantly contributes to the pFIMP direct search cross section. Notably, $\sigma_{\chi_2}^{\rm eff}$ also depends on the mass splitting Δm and pFIMP relic density $\Omega_{\chi_2}h^2$, which is small for large conversion rate. The different thick (dashed) colored lines correspond to existing (projected) bounds from the different experiments mentioned in the figure inset. Essentially, the part of relic density-allowed parameter space with $\lambda_{1H} \gtrsim 0.5$ is under conflict with DD limits.

4. Indirect detection limits on WIMPs and pFIMPs

The limit on DM self-annihilation into $b\bar{b}, W^+W^-, ZZ$, and $t\bar{t}$ is obtained from the data of the *Fermi* collaboration

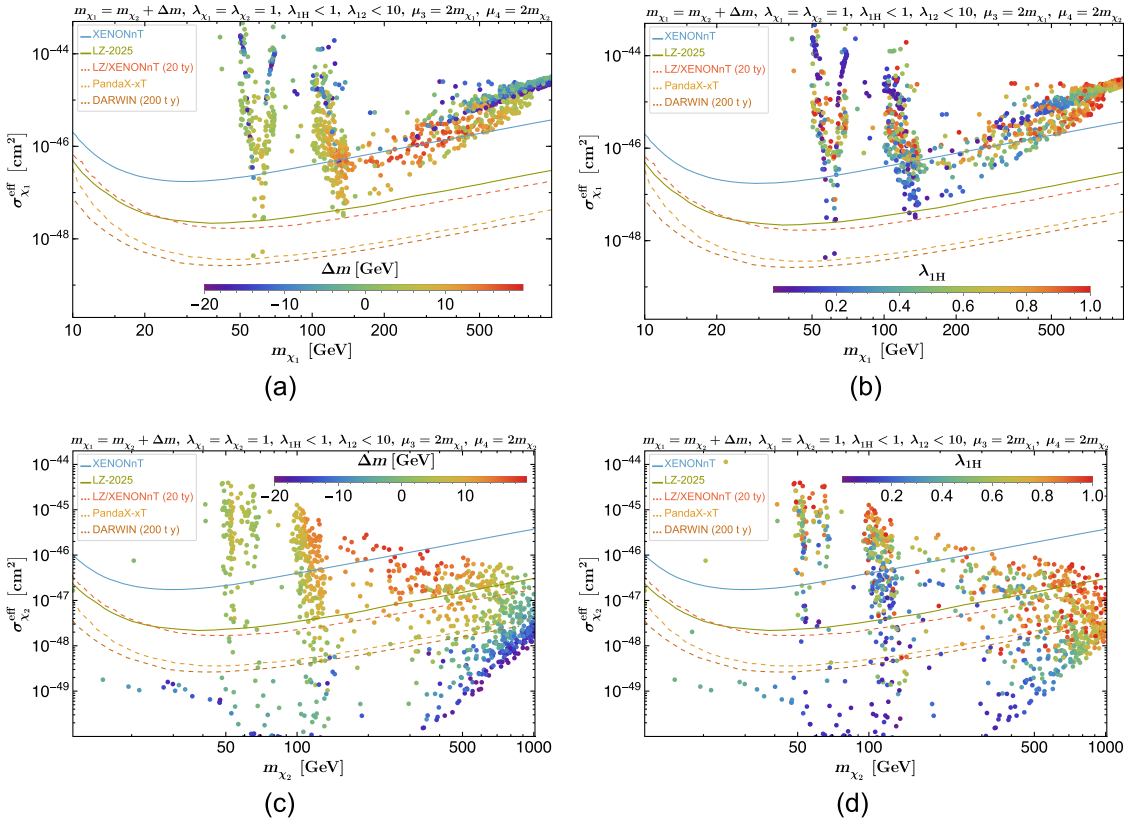


FIG. 3. In panels (a)–(d), we have shown the relic density-allowed parameter space of the two-component WIMP-pFIMP setup on the $m_{\chi_1} - \sigma^{\rm eff}_{\chi_1}$ (top panel) and $m_{\chi_2} - \sigma^{\rm eff}_{\chi_2}$ planes (bottom panel). We have taken $\lambda'_{12} = \lambda_3 = \lambda_4 = 10^{-20}$ and $\mu_1 = \mu_2 = 10^{-15}$ GeV to stabilize χ_2 and choose $\lambda_{2H} = 10^{-12}$ to make χ_2 a pFIMP. Other parameters kept fixed or varied are shown in the figure heading and inset.

from 6 years of observation of 15 dSphs [48]. They also provide projected sensitivity for 45 dSphs of 16 years of observation [49]. Various gamma-ray observations from *Fermi*-LAT [48], H.E.S.S. [51], and CTA [55] put a bound on DM semiannihilation $\chi_i\chi_i \to \chi_i^* h$. We will calculate both the self- and semiannihilation rates in this two-component WIMP-pFIMP setup and apply the bounds to find allowed parameter space that can be probed further.

The effective WIMP (χ_1) self- and semiannihilation cross sections are given by

$$\langle\sigma v\rangle^{\rm eff}_{\chi_1\chi_1^*\to b\bar{b}} = \left(\frac{\Omega_{\chi_1}h^2}{\Omega_{\chi_1}h^2+\Omega_{\chi_2}h^2}\right)^2 \langle\sigma v\rangle_{\chi_1\chi_1^*\to b\bar{b}} \quad (4.16)$$

and

$$\langle\sigma v\rangle^{\rm eff}_{\chi_1\chi_1\to\chi_1^* h} = \left(\frac{\Omega_{\chi_1}h^2}{\Omega_{\chi_1}h^2+\Omega_{\chi_2}h^2}\right) \langle\sigma v\rangle_{\chi_1\chi_1\to\chi_1^* h}. \quad (4.17)$$

In Eqs. (4.16) and (4.17), the thermal average of self- and semiannihilation cross sections are evaluated at the WIMP freeze-out point, $T^{\rm FO}_{\chi_1} \sim m_{\chi_1}/25$, and plotted in the $m_{\chi_1} - \langle\sigma v\rangle^{\rm eff}_{\chi_1\chi_1^*\to b\bar{b}}$ plane in Figs. 4(a) and 4(c), respectively. The rainbow color bar shows the spin-independent direct detection cross section of pFIMPs in cm^2 units. The effective self- and semiannihilation cross section of WIMPs depend on λ_{1H}, WIMP mass, and the effective WIMP contribution to the total DM relic. *Fermi*-LAT observation and projection data are shown by thick gray and dashed green lines, respectively. We see that most of the parameter space probed here obeys the limit.

The pFIMP χ_2 connects with the visible sector via WIMP loop-mediated interaction, as shown in Figs. 2(g) to 2(j). These diagrams are subdominant to the tree-level processes. The effective self-annihilation cross section of pFIMPs (χ_2) is given by

$$\langle\sigma v\rangle^{\rm eff}_{\chi_2\chi_2^*\to b\bar{b}} = \left(\frac{\Omega_{\chi_2}h^2}{\Omega_{\chi_1}h^2+\Omega_{\chi_2}h^2}\right)^2 \langle\sigma v\rangle_{\chi_2\chi_2^*\to b\bar{b}}, \quad (4.18)$$

and the pFIMP semiannihilation cross section is given by

$$\langle\sigma v\rangle^{\rm eff}_{\chi_2\chi_2\to\chi_2^* h} = \left(\frac{\Omega_{\chi_2}h^2}{\Omega_{\chi_1}h^2+\Omega_{\chi_2}h^2}\right) \langle\sigma v\rangle_{\chi_2\chi_2\to\chi_2^* h}. \quad (4.19)$$

The dominant self-annihilation of χ_2 to SM pair comes from Fig. 2(g), while others are suppressed due to tiny couplings assumed for the stability of χ_2. We also need to

remove the divergence contribution from the vertex correction diagram, Fig. 2(g). We take $q_h^2 = 4m_{\chi_2}^2$ as our renormalization scale [42]. Then, we calculate the thermal average annihilation cross section at the pFIMP freeze-out point, $T_{\chi_2}^{FO} \sim m_{\chi_2}/25$.

Figures 4(b) and 4(d) show the relic density-allowed parameter space in the $m_{\chi_2} - \langle\sigma v\rangle^{\rm eff}_{\chi_2\chi_2^*\to b\bar{b}}$ and $m_{\chi_2} - \langle\sigma v\rangle^{\rm eff}_{\chi_2\chi_2\to\chi_2^* h}$ planes, respectively. The pFIMP effective semiannihilation cross section is written in Eq. (4.19) and is proportional to the λ_{1H}, λ_{12}, and μ_4 couplings. Among these three, λ_{1H} and λ_{12} contribute to the pFIMP DD cross section. With larger λ_{1H}, both the self-annihilation and direct detection cross section of pFIMPs increase, which is also reflected in Fig. 4(b). Finally, we constrain the parameter space by imposing the *Fermi*-LAT observation and projection bound in the $m_{\chi_2} - \langle\sigma v\rangle^{\rm eff}_{\chi_2\chi_2^*\to b\bar{b}}$ plane, and the color bar represents the variation in the effective pFIMP direct detection cross section. The pFIMP semiannihilation

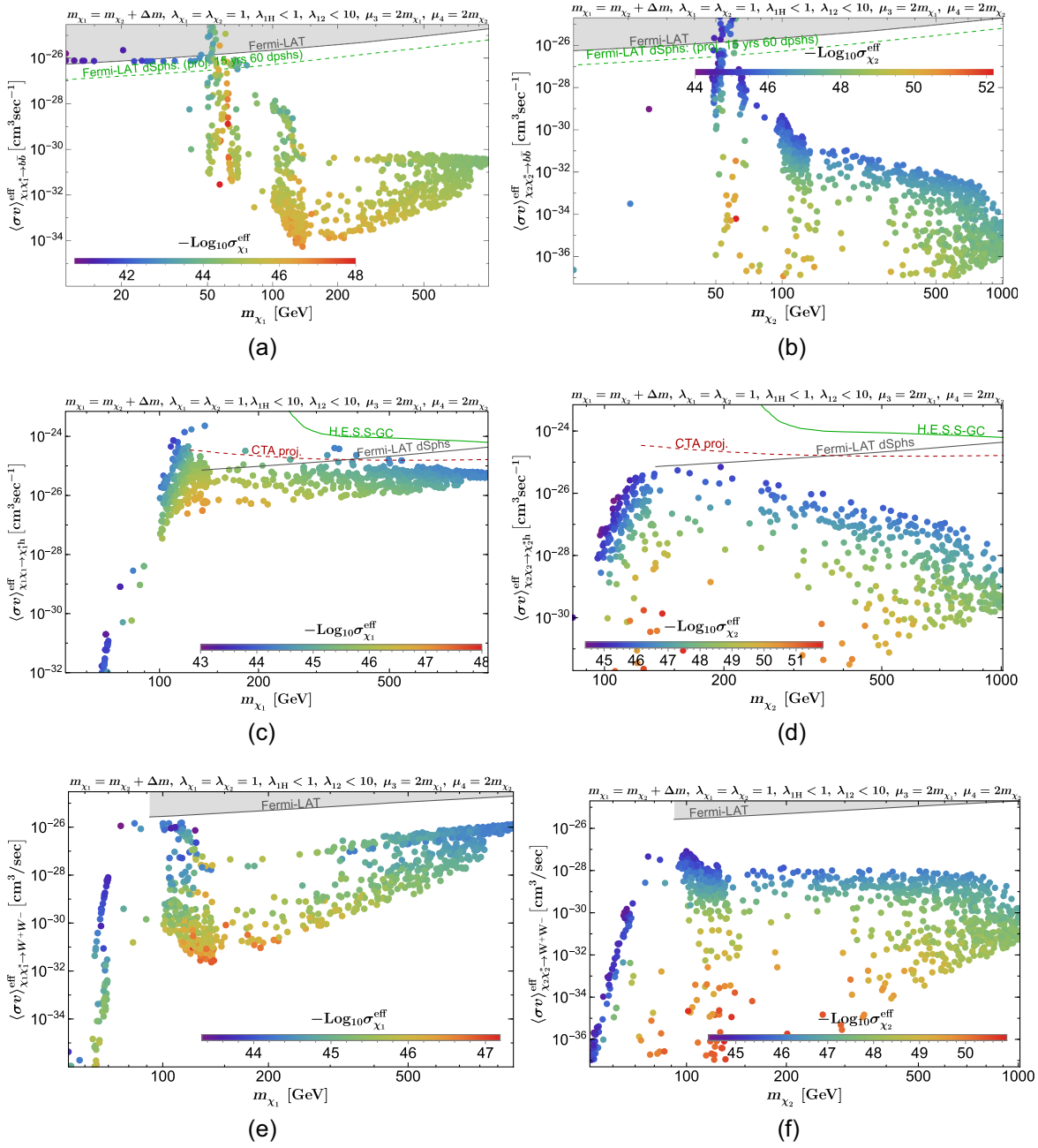


FIG. 4. Panels (a) [(e)] and (b) [(f)] show the relic-allowed parameter space $m_{\chi_1} - \langle\sigma v\rangle^{\rm eff}_{\chi_1\chi_1^*\to b\bar{b}(W^+W^-)}$ and $m_{\chi_2} - \langle\sigma v\rangle^{\rm eff}_{\chi_2\chi_2^*\to b\bar{b}(W^+W^-)}$ plane, respectively, for WIMPs and pFIMPs, while panels (c),(d) correspond to WIMP and pFIMP semiannihilation. We have taken $\lambda'_{12} = \lambda_3 = \lambda_4 = 10^{-20}$ and $\mu_1 = \mu_2 = 10^{-15}$ GeV to stabilize the heavier DM and $\lambda_{2H} = 10^{-12}$ to become χ_2 as pFIMPs.

is also mediated via the WIMP loop; see Figs. 2(h) to 2(j). We have used the bound on DM semiannihilation from H.E.S.S (green), *Fermi*-LAT (gray), and CTA (dashed red) in Fig. 4(d). These constraints exclude some regions, which are also excluded by the presently available DD bounds.

In summary, the two-component DM scenario of type A after stabilizing the heavier component by adjusting coupling parameters behaves like the $\mathcal{Z}_3 \otimes \mathcal{Z}_3'$ scenario. Additionally, when the heavier DM component behaves like pFIMPs having tiny portal interaction, the underabundant parameter space of WIMPs is adequately utilized by the second component and enhances the allowed parameter space. Having the second component as pFIMPs reduces the DD and ID bounds, as they are primarily governed by loop-mediated interactions, and allows one to exploit a larger parameter space compared to the WIMP-WIMP case [82]. Both DM components are allowed within the GeV to TeV range, where semiannihilation and conversion play crucial roles for yielding correct DM relic density.

5. Scenario B

In scenario B (Table III), the absence of χ_2^3 helps in the stabilization of the heavier particle. This parameter does not have any significance in the WIMP-pFIMP setup. But the presence of $\chi_1^2\chi_2^2$ and $\chi_2^2\chi_1^*$ terms has an important role in the semiannihilation of χ_2 for the WIMP-WIMP scenario. They open up many conversion and semiconversion channels, shown in Fig. 12, which are absent in scenario A or the WIMP-WIMP setup under the $\mathcal{Z}_3 \otimes \mathcal{Z}_3'$ model. We will do a similar kind of analysis to understand the benefits, similar to scenario A. We study both (1) WIMP-WIMP ($\lambda_{2H} \neq 0$) and (2) WIMP-pFIMP ($\lambda_{2H} \to 0$) cases below.

6. WIMP-WIMP

In the case of a real scalar singlet WIMP as a single component DM, some breathing space is left near the Higgs resonance region or in the high mass regime, $\gtrsim$1 TeV, but the direct detection sensitivity is less for the latter. In the two-component real scalar singlet WIMP scenario, the choices could be (1) one is near Higgs resonance, and another in the higher mass regime, $m_{\rm DM} \gtrsim 1$ TeV, or (2) both DM masses are far above the Higgs resonance. In scenario B, the presence of the χ_1^3 term opens up semiannihilation channels, which brings more relic- and DD-allowed parameter space.

However, in the two-component complex scalar WIMP scenario as here, χ_2 semiannihilation is inefficient due to the feeble χ_2^3, but it opens the door for conversion and semiconversion channels via $\chi_1^2\chi_2^2$ and $\chi_2^2\chi_1^*$ terms. Along with the standard DM-DM conversion via the $|\chi_1|^2|\chi_2|^2$ term, we then have χ_1 semiannihilation ($\chi_1\chi_1 \to \chi_1^* h$) due to χ_1^3 and χ_2 mediated DM-DM conversion [Figs. 12(h) and 12(k)] and semiconversion ($\chi_2\chi_2 \to \chi_1^* h$) [Figs. 12(m) and 12(n)] due to the presence of the $\chi^2\chi_1^*$ term, all of which help in acquiring the correct relic without perturbing the DD or ID searches. The $\chi_1 - \chi_2$ conversion can also be possible via Higgs mediation and χ_2 mediation along with the four-point scattering. So, the Higgs resonance effect is not only limited to DM annihilation to SM particles but also to DM-DM conversion. The s-channel semiconversion of $\chi_2\chi_2 \to \chi_1^* h$ is more effective near the Higgs mass regime. These processes help to relax the Higgs portal coupling but keep adequate depletion via conversion processes and save the DM components from DD constraints. In Fig. 5, we have shown the relic density-allowed parameter space and incorporated possible direct detection bounds. Figure 5(a) represents the relic-allowed parameter space in the $m_{\chi_1} - m_{\chi_2}$ plane, while the rainbow color bar shows the variation in percentage contribution of χ_1 in the total relic. If $m_{\chi_1} > m_{\chi_2}$, then the χ_1 relic is subdominant due to conversion of χ_1 to χ_2, decreasing the χ_1 number density, but the χ_2 number density is enhanced simultaneously. Around the Higgs resonance and semiannihilation region, the conversion effect could be ignored, and equal contribution arises; see the green color points in Fig. 5(a). Figures 5(b) and 5(c) represent the relic-allowed point in the $m_{\chi_1} - \sigma_{\chi_1}^{\rm eff}$ and $m_{\chi_2} - \sigma_{\chi_2}^{\rm eff}$ plane, respectively. In Fig. 5(b), we see two kinks, m_{χ_1}, around the Higgs resonance and Higgs-mass region, where the semiannihilation process is more effective because of the presence of the χ_1^3 term. Beyond the Higgs mass, semiannihilation and the self-annihilation cross section decrease, which can be adjusted by λ_{1H} and λ_{12}, but λ_{1H} is strongly restricted by DD. On the contrary, as the trilinear coupling of χ_2 is very tiny to keep it stable, there is no kink due to semiannihilation near the Higgs mass in Fig. 5(d). So, with larger mass, the decrease in cross section is adjusted by the enhancement of λ_{2H}. Although semiannihilation of χ_2 is not active in the absence of the χ_2^3 term, semiconversion channels are there due to $\chi_2^2\chi_1^*$ terms, which help to relax the λ_{2H} coupling. In Fig. 5(d), we show the effect of conversion in the $m_{\chi_1} - m_{\chi_2}$ plane.

The main outcome of this scenario is that we are getting relic- and DD-allowed points near the Higgs resonance, Higgs mass, and also some above the Higgs mass, represented by the green stars in Fig. 5. Indirect search limits are less stringent than DD and do not alter the allowed parameter space.

7. WIMP-pFIMP

In scenario B (Table III), we have identified χ_2 as pFIMP by choosing $\lambda_{2H} \sim 10^{-12}$, so that it does not have a direct SM connection; however, sizable λ_{12} keeps it in thermal bath via interaction with χ_1.

The relic density in the WIMP-pFIMP limit is calculated by solving a coupled BEQ using MICROMEGAS [99]; for relevant Feynman diagrams related to annihilation, semiannihilation, and conversion channels, see Fig. 12. The WIMP and pFIMP relic density-allowed parameter spaces are shown in Figs. 7 and 8. As before, the direct and indirect

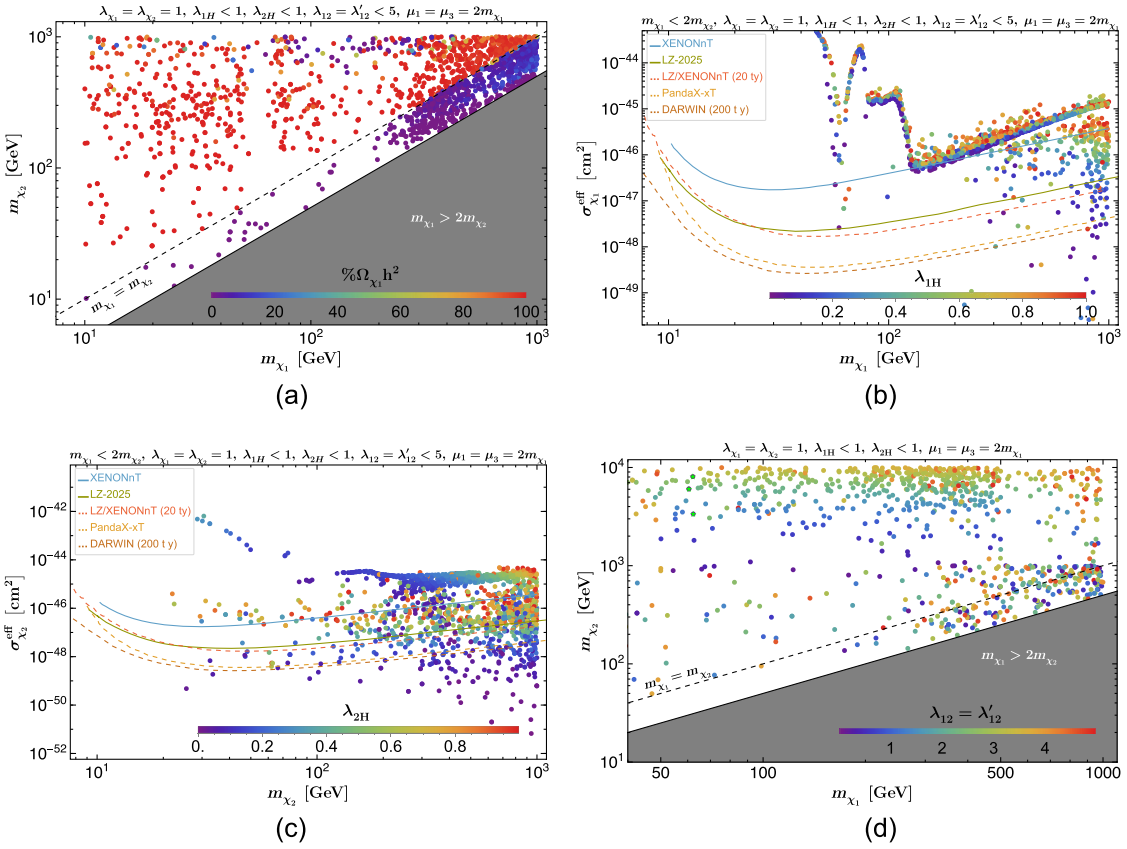


FIG. 5. Panels (b) and (c) show the relic density-allowed parameter space for two-component WIMPs in category B (Table III) in the $m_{\chi_1} - \sigma^{\rm eff}_{\chi_1}$ and $m_{\chi_2} - \sigma^{\rm eff}_{\chi_2}$ planes, respectively. Panels (a) and (d) show the relic-allowed parameter space in the $m_{\chi_1} - m_{\chi_2}$ plane, where the rainbow color depicts variations in $\Omega_{\chi_1} h^2$ and λ_{12}. The couplings $(\mu_2, \mu_4, \lambda_3, \lambda_4)$ are taken adequately small $(\sim 10^{-20})$ to stabilize the heavier DM component. The gray-shaded region is excluded from the heavier particle stability. In panel (d), the green star points depict the case where both DM components obey the stringent limit on the spin-independent DM-nucleon scattering cross section from LZ-2025.

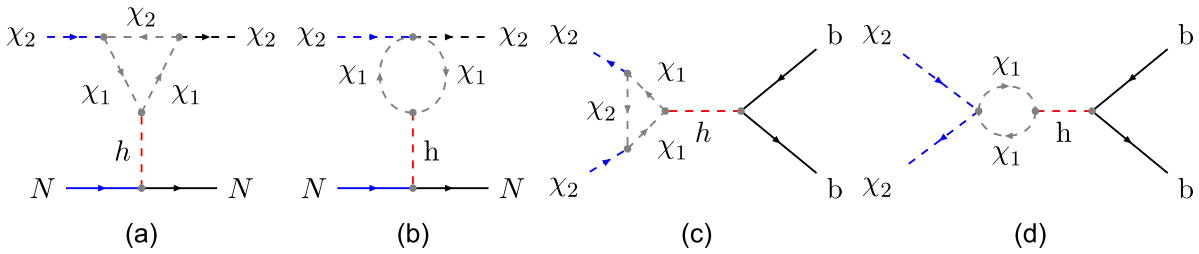


FIG. 6. Panels (a) and (b), (c) and (d) represent the Feynman diagrams related to the direct and indirect detection of pFIMPs (χ_2), respectively.

detection of WIMPs is possible through the Higgs portal λ_{1H}, but the pFIMP detection is possible only via the WIMP loop-mediated diagrams; see Fig. 6. The loop divergences have been taken care of using the on-shell renormalization scheme, while the renormalization scale is chosen at $\sim 4m^2_{\chi_2}$.

Figure 7 shows the WIMP and pFIMP relic density-allowed parameter space in the $m_{\chi_1} - \sigma^{\rm eff}_{\chi_1}$, $m_{\chi_2} - \sigma^{\rm eff}_{\chi_2}$ planes, and the color bar shows the variation in different relevant parameters, as mentioned in the figure insets. The different colored lines correspond to the lower bounds from different direct detection experiments, while thick and dashed lines represent the observed and projected limits on the spin-independent DM-nucleon scattering cross section. We see that along with the Higgs resonance, the semiannihilation region is also available. One important point to note is that we can also have ∼500 GeV WIMP mass, where the mass splitting $|\Delta m|$ can go up to 100 GeV;

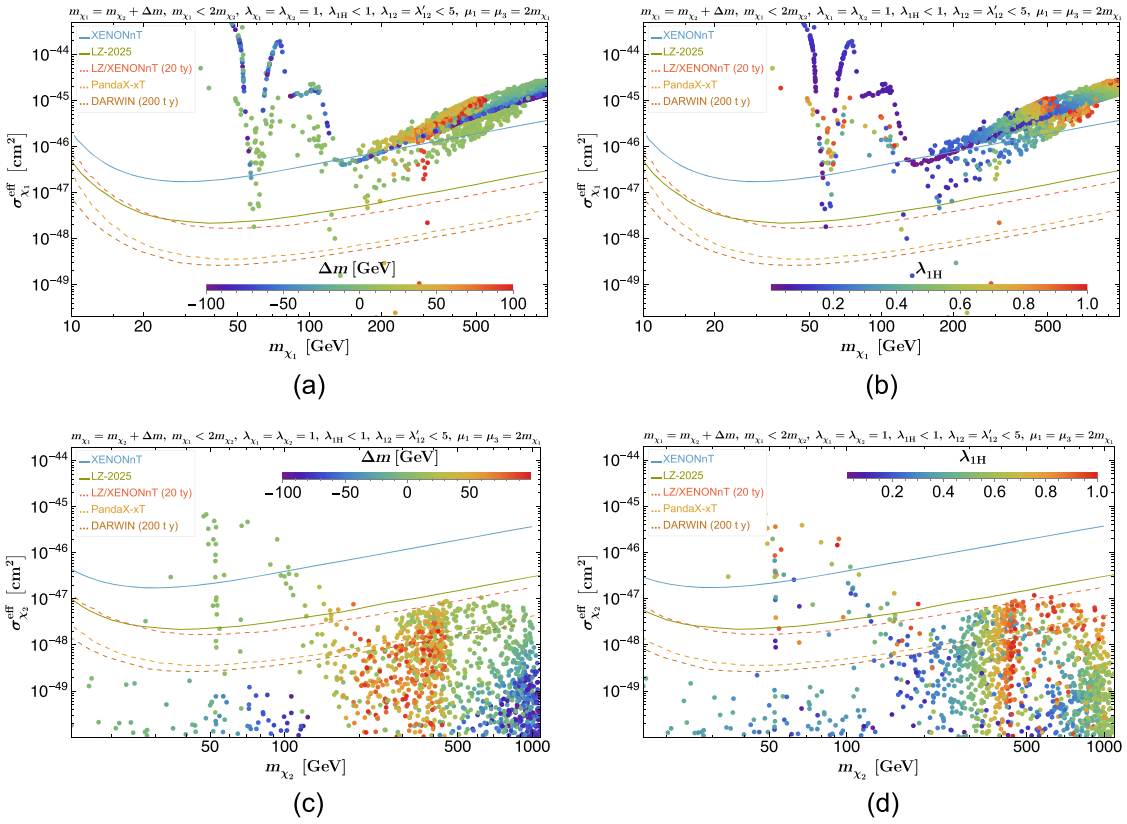


FIG. 7. Panels (a)–(d) show the relic density-allowed parameter space in the $m_{\chi_1} - \sigma^{\rm eff}_{\chi_1}$ and $m_{\chi_2} - \sigma^{\rm eff}_{\chi_2}$ planes, respectively. The couplings $(\mu_2, \mu_4, \lambda_3, \lambda_4)$ are taken adequately small to stabilize the heavier DM χ_2 so that it falls in category B of two-component DM (Table III). The rainbow color bar shows the variation in Δm (left) and λ_{1H} (right). The thick and dashed lines correspond to the lower limits on the observed and projected DM-nucleon spin-independent DD cross section, respectively, while different colors refer to the experiments as mentioned in the figure inset.

see Fig. 7(c). This is unlike the 5 GeV mass splitting for the two real scalar WIMP-pFIMP DM scenario [42]. The reason for this is the presence of an additional semi-conversion channel $\chi_2\chi_2 \to \chi_1^* h$ [Fig. 12(m)] here, which is strongly active when $m_{\chi_1} \sim m_h$. Figure 7(d) shows the relic density-allowed parameter space in $m_{\chi_2} - \sigma^{\rm eff}_{\chi_2}$, and the color bar shows the variation in WIMP-Higgs portal coupling (λ_{1H}). The pFIMP-nucleon cross section is directly proportional to $(\mu_1,\ \lambda_{12},\ \lambda_{1H})$ and depends on the WIMP and pFIMP masses via loop factor and on the effective relic density contribution. For this reason, around the Higgs-resonance regime, the WIMP relic is very small compared to pFIMP, and the effective relic contribution decreases with larger pFIMP mass, as visible in Fig. 7(c).

Figure 8 shows the indirect detection limit on the DM self-annihilation and semiannihilation in the relic-allowed parameter space of the WIMP-pFIMP setup. *Fermi*-LAT, H.E.S.S, and CTA put limits on the annihilation of WIMPs and pFIMPs into $b\bar{b}$. Figures 8(a) and 8(b) show the relic-allowed parameter space in the $m_{\chi_1} - \langle\sigma v\rangle^{\rm eff}_{\chi_1\chi_1^* \to b\bar{b}}$ and $m_{\chi_2} - \langle\sigma v\rangle^{\rm eff}_{\chi_2\chi_2^* \to b\bar{b}}$ planes, while the color bar shows the variation in $-{\rm Log}_{10}\sigma^{\rm eff}_{\chi_1}$ and $-{\rm Log}_{10}\sigma^{\rm eff}_{\chi_2}$, respectively. For both the plots, near Higgs resonance, some points are disallowed by the *Fermi*-LAT data. Semiannihilation bounds from indirect searches are not applicable to pFIMPs due to the absence of the χ_2^3 term. Figure 8(f) shows relic density-allowed points in the $m_{\chi_1} - m_{\chi_2}$ plane, where the gray-shaded region is excluded by the DM decay kinematics. The relic- and DD-allowed points, denoted by green stars, lie in the vicinity of the mass degenerate line. This is in contrast to the WIMP-WIMP situation described before [see Fig. 5(d)].

V. SUMMARY AND CONCLUSION

DM is well motivated from several observations but is yet undiscovered. Single component DM frameworks are often constrained heavily from relic density and DD/ID bounds, as the processes that govern them are essentially the same, but one requires adequate depletion of weak interaction strength to satisfy correct relic density but very tiny interaction for direct search from nonobservation of DM. Multipartite DM frameworks go beyond the simplistic assumption of being constituted of a single particle and offer many dynamical possibilities and a larger parameter

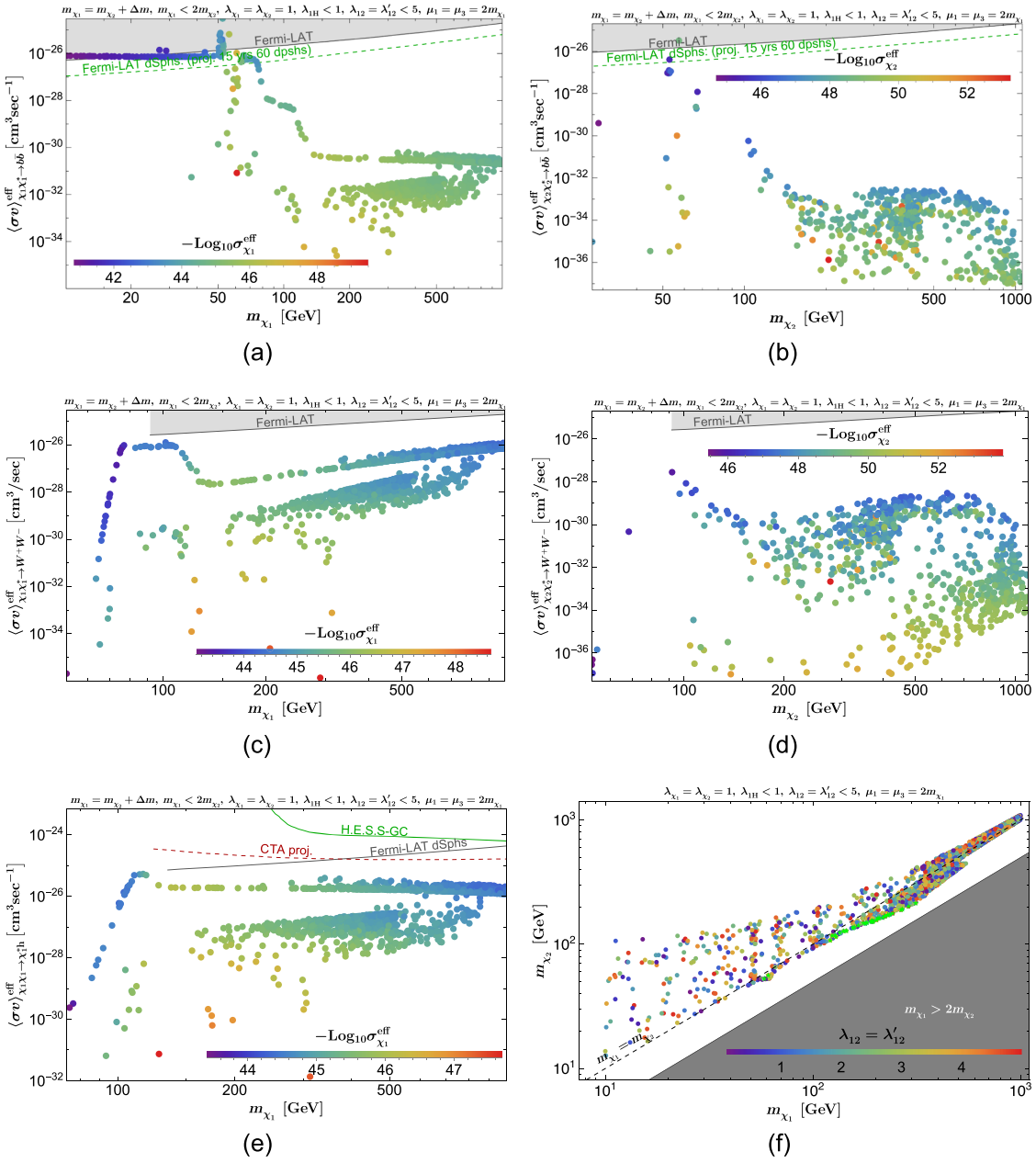


FIG. 8. Panels (a), (c) and (b), (d) represent the indirect detection limit on the self-annihilation of WIMPs and pFIMPs into the $\to b\bar{b}(W^+W^-)$ channel in the relic density-allowed parameter space, respectively. Panel (e) shows the indirect observational constraints on the WIMP semiannihilation. In panel (f), we show the relic density-allowed parameter space in the $m_{\chi_1} - m_{\chi_2}$ plane, where WIMP and pFIMP DD- and ID-allowed points are indicated by green stars. The thick and dashed lines correspond to the observed and projected limits of the experiments as mentioned in the figure(s).

space to be explored, as the depletion process can be segregated from the direct/indirect/collider interactions. Achieving a stable DM candidate requires extra symmetries to be imposed under which DM transforms nontrivially, but SM is a singlet. On the other hand, multicomponent DM requires more than one stabilizing symmetry most often.

The motivation of our study is to find the possible multicomponent DM frameworks when SM is extended with more than one scalar field but transforming under a single symmetry. Such efforts have already been done in many papers; however, under what circumstances such scenarios evolve has not been elaborated systematically. The heavier components usually have decay terms to DM and to SM. In our paper, we show that the stabilization of the heavier component depends strictly on the charges of the dark fields under symmetry transformation. For example, whenever, under $\mathcal{Z}_N$ symmetry, $q_1 \neq q_2, q_1 + q_2 \neq N$, the heavier component decays only to a dark sector particle,

thus allowing it to be stabilized by imposing simple kinematical constraint. However, if the above condition on dark sector particle charges is not obeyed, then the heavier component can decay to both DM and SM. Such decays at the tree-, one-loop, and two-loop levels can be stopped only when we make some couplings vanishingly small. After that, the scenario either resembles the $\mathcal{Z}_N \otimes \mathcal{Z}'_N$ case or the $q_1 \neq q_2, q_1 + q_2 \neq N'$ case of a $\mathcal{Z}_{N'}$ group, where $N' > N$. We have explicitly demonstrated all the possibilities for having two DM components in $\mathcal{Z}_2$, $\mathcal{Z}_3$, and $\mathcal{Z}_4$ symmetric cases. We should note here that there is no choice pertaining to $q_1 \neq q_2, q_1 + q_2 \neq N$ for the $\mathcal{Z}_2$ and $\mathcal{Z}_3$ symmetric cases, forcing us to compromise some of the couplings of these models to make the heavier DM component stable.

We specifically elaborate the phenomenology associated with $\mathcal{Z}_3$. Interestingly, the choices of terms that should be neglected (or assumed small) are not unique. This gives rise to different possible scenarios in $\mathcal{Z}_3$ symmetry after stabilizing the heavier component. For example, one can have $\mathcal{Z}_3 \otimes \mathcal{Z}'_3$ or $\mathcal{Z}_6$ with $\{q_1, q_2\} = \{2, 5\}, \{4, 1\}$, etc. They also provide different phenomenological implications. In this article, we have discussed two such examples. Conversion, semiconversion, and semiannihilation are some of the key processes that dictate the allowed parameter space of the two-component DM model and their compatibility with DD/ID searches. Note that after the heavy particle becomes a stable DM candidate, the coannihilation process stops contributing. This reduces the allowed parameter space of the model, particularly to comply with nonobservation of DM in DD/ID experiments.

Further, the two DM components can be WIMPs or pFIMPs depending on the strength of the corresponding Higgs portal couplings. Both the WIMP-WIMP case and the WIMP-pFIMP case are illustrated here, and we show that the WIMP-pFIMP case enjoys a larger parameter space, as the pFIMP detection relies on loop-level WIMP mediated interactions. There is another interesting feature that comes out of the specific WIMP-pFIMP analysis in $\mathcal{Z}_3$ symmetry, that here, the pFIMP not only relies on conversion with WIMP to thermalize, but also, semiconversion plays a crucial role for the same, which makes a crucial distinction that one can choose a large mass splitting between WIMPs and pFIMPs, unlike the $\mathcal{Z}_2$ case with two real scalars [42]. This, in turn, can help distinguishing WIMPs and pFIMPs in direct search and collider search experiments via a kink or a double hump missing energy distribution, which is otherwise difficult with smaller mass splitting. We will discuss that possibility elsewhere.

ACKNOWLEDGMENTS

D. P. thanks Heptagon, IITG for useful discussions.

DATA AVAILABILITY

There are no publicly available research data or software supporting this manuscript. Requests for further information or data should be sent to the authors.

APPENDIX A: KINETIC MIXING

The SM extended Lagrangian containing two complex scalar fields, χ_1^0 and χ_2^0, which transform under the $\mathcal{Z}_3$ symmetry as $\chi_1^0 \to \omega\chi_1^0$ and $\chi_2^0 \to \omega^2\chi_2^0$, is given by

$$\mathcal{L} = \mathcal{L}_{\rm SM} + \mathcal{L}^{\rm kin}_{\chi_1^0\chi_2^0} + \mathcal{L}^{\rm mass}(\chi_1^0, \chi_2^0) + \mathcal{L}^{\rm int}(\chi_1^0, \chi_2^0, H). \quad \text{(A1)}$$

The kinetic Lagrangian contains a noncanonical kinetic mixing term,

$$\mathcal{L}^{\rm kin}_{\chi_1^0\chi_2^0} = (\partial_\mu\chi_1^0)^\dagger(\partial^\mu\chi_1^0) + (\partial_\mu\chi_2^0)^\dagger(\partial^\mu\chi_2^0) + \kappa(\partial_\mu\chi_1^0)(\partial^\mu\chi_2^0) + \kappa(\partial_\mu\chi_1^0)^\dagger(\partial^\mu\chi_2^0)^\dagger, \quad \text{(A2)}$$

where $|\kappa| < 1$ is required for the kinetic matrix to be positive definite. For simplicity, we also assume that κ is real. The presence of the holomorphic kinetic mixing term prevents the kinetic matrix from being diagonal. Therefore, the first step is to identify a field basis in which the kinetic sector becomes diagonal.[4]

The quadratic part of the scalar potential is given by

$$\mathcal{L}^{\rm mass}_{\chi_1^0\chi_2^0} = \underbrace{\left(\mu_{11}^2 + \frac{1}{2}\lambda_{1H}^0 v^2\right)}_{m_{11}^2}(\chi_1^0)^\dagger(\chi_1^0) + \underbrace{\left(\mu_{22}^2 + \frac{1}{2}\lambda_{2H}^0 v^2\right)}_{m_{22}^2}(\chi_2^0)^\dagger(\chi_2^0) + \underbrace{\frac{1}{2}\left(\mu_{12}^2 + \frac{1}{2}\lambda_{12H} v^2\right)}_{m_{12}^2}(\chi_1^0\chi_2^0) + \underbrace{\frac{1}{2}\left(\mu_{12}^2 + \frac{1}{2}\lambda_{12H} v^2\right)}_{m_{12}^2}(\chi_1^0)^\dagger(\chi_2^0)^\dagger$$
$$= m_{11}^2(\chi_1^0)^\dagger(\chi_1^0) + m_{22}^2(\chi_2^0)^\dagger(\chi_2^0) + m_{12}^2(\chi_1^0\chi_2^0) + m_{12}^2(\chi_1^0)^\dagger(\chi_2^0)^\dagger, \quad \text{(A3)}$$

[4]We refer to this as a holomorphic kinetic mixing term because it mixes two fields with identical gauge quantum numbers through a bilinear of the form $\chi_1^0\chi_2^0$, rather than through a Hermitian combination involving a field and its conjugate. This terminology is analogous to the holomorphic bilinears that appear in supersymmetric theories [103–105].

$$\mathcal{L}^{\rm int}(\chi_1^0,\chi_2^0,H) = +\lambda_{\chi_1}^0|\chi_1^0|^4 + \lambda_{\chi_2}^0|\chi_2^0|^4 + \lambda_{1H}^0|\chi_1^0|^2(\mathrm{H}^\dagger H - v^2/2) + \lambda_{2H}^0|\chi_2^0|^2(\mathrm{H}^\dagger H - v^2/2) + \lambda_{12}^0|\chi_1^0|^2|\chi_2|^2 + \frac{1}{2}\lambda_{12H}^0(\chi_1^0\chi_2^0 + \mathrm{H.c.})(\mathrm{H}^\dagger H - v^2/2) + \frac{1}{2}\lambda_{12}^{0\prime}[(\chi_1^0\chi_2^0)^2 + \mathrm{H.c.}] + \frac{1}{2}[\lambda_3^0\chi_1^0\chi_2^0|\chi_1^0|^2 + \lambda_4^0\chi_1^0\chi_2^0|\chi_2^0|^2 + \mathrm{H.c.}] + \frac{1}{2}[\mu_1^0(\chi_1^0)^*(\chi_2^0)^2 + \mu_2^0(\chi_1^0)^2(\chi_2^0)^* + \mu_3^0(\chi_1^0)^3 + \mu_4^0(\chi_2^0)^3 + \mathrm{H.c.}]. \tag{A4}$$

1. Kinetic diagonalization

$$\begin{pmatrix} \chi_1^0 \\ (\chi_2^0)^\dagger \end{pmatrix} = \frac{1}{\sqrt{2}}\begin{pmatrix} 1 & -1 \\ 1 & 1 \end{pmatrix}\begin{pmatrix} H_1 \\ H_2 \end{pmatrix} \tag{A5}$$

We introduce the field redefinitions [105–108]

$$\chi_1^0 = \frac{H_1 - H_2}{\sqrt{2}}, \qquad (\chi_2^0)^\dagger = \frac{H_1 + H_2}{\sqrt{2}}, \tag{A6}$$

or, equivalently,

$$H_1 = \frac{\chi_1^0 + (\chi_2^0)^\dagger}{\sqrt{2}}, \qquad H_2 = \frac{(\chi_2^0)^\dagger - \chi_1^0}{\sqrt{2}}. \tag{A7}$$

Substituting Eq. (A6) into Eq. (A2) yields

$$\mathcal{L}_{H_1H_2}^{\rm kin} = (1+\kappa)\partial_\mu H_1^\dagger \partial^\mu H_1 + (1-\kappa)\partial_\mu H_2^\dagger \partial^\mu H_2. \tag{A8}$$

The kinetic mixing has, therefore, been eliminated. However, the kinetic terms are not yet canonically normalized.

a. Canonical normalization

To obtain canonical kinetic terms, we perform the rescaling

$$H_1 = \sqrt{2}\kappa_+ h_1, \qquad H_2 = \sqrt{2}\kappa_- h_2, \tag{A9}$$

where $\kappa_\pm = \frac{1}{\sqrt{2(1\pm\kappa)}}$. Substituting Eq. (A9) into Eq. (A8) gives

$$\mathcal{L}_{h_1h_2}^{\rm kin} \equiv (\partial_\mu h_1)^\dagger \partial^\mu h_1 + (\partial_\mu h_2)^\dagger \partial^\mu h_2, \tag{A10}$$

which is the desired canonical form. At this stage, the kinetic sector has been completely diagonalized and canonically normalized.

2. Mass terms in the canonical basis

The next step is to rewrite the quadratic scalar potential in terms of the canonically normalized fields. Using Eqs. (A6) and (A9), the potential in Eq. (A3) becomes

$$\mathcal{L}_{\chi_1^0\chi_2^0}^{\rm mass} \Rightarrow \mathcal{L}_{h_1h_2}^{\rm mass} = \kappa_+^2(m_{11}^2 + 2m_{12}^2 + m_{22}^2)h_1h_1^\dagger + \kappa_-^2(m_{11}^2 - 2m_{12}^2 + m_{22}^2)h_2h_2^\dagger + \kappa_+\kappa_-(m_{22}^2 - m_{11}^2)(h_1h_2^\dagger + h_2h_1^\dagger) \tag{A11}$$

The mass-mixing matrix can be written as

$$\mathbb{M}_{h_1h_2} = \begin{pmatrix} \kappa_+^2(m_{11}^2 + 2m_{12}^2 + m_{22}^2) & \kappa_+\kappa_-(m_{22}^2 - m_{11}^2) \\ \kappa_+\kappa_-(m_{22}^2 - m_{11}^2) & \kappa_-^2(m_{11}^2 - 2m_{12}^2 + m_{22}^2) \end{pmatrix}. \tag{A12}$$

The mass terms can be written in matrix form as

$$\mathcal{L}_{h_1h_2}^{\rm mass} = (\,h_1^\dagger \qquad h_2^\dagger\,)\mathbb{M}_{h_1h_2}\begin{pmatrix} h_1 \\ h_2 \end{pmatrix}. \tag{A13}$$

To diagonalize the mass matrix, we give the following rotation to the canonically normalized fields:

$$\begin{pmatrix} h_1 \\ h_2 \end{pmatrix} = \begin{pmatrix} \cos\theta & -\sin\theta \\ \sin\theta & \cos\theta \end{pmatrix}\begin{pmatrix} \chi_1 \\ \chi_2^\dagger \end{pmatrix}, \tag{A14}$$

where the mixing angle θ can be given by

$$\tan 2\theta = \frac{2\kappa_+\kappa_-(m_{22}^2 - m_{11}^2)}{(m_{11}^2 + m_{22}^2)(\kappa_+^2 - \kappa_-^2) + 2m_{12}^2(\kappa_+^2 + \kappa_-^2)}, \tag{A15}$$

and the diagonalized fields have the physical mass

$$m_{\chi_{1,2}}^2 = \frac{1}{2}\Big[(\mathbb{M}_{h_1h_2}^{11})^2 + (\mathbb{M}_{h_1h_2}^{22})^2 \mp \sqrt{((\mathbb{M}_{h_1h_2}^{11})^2 - (\mathbb{M}_{h_1h_2}^{22})^2)^2 + 4(\mathbb{M}_{h_1h_2}^{12})^4}\Big]. \tag{A16}$$

Therefore, the old basis in terms of the new physical basis can be written as

$$\begin{pmatrix} \chi_1^0 \\ (\chi_2^0)^\dagger \end{pmatrix} = \underbrace{\begin{pmatrix} \kappa_+ & -\kappa_- \\ \kappa_+ & \kappa_- \end{pmatrix}\begin{pmatrix} \cos\theta & -\sin\theta \\ \sin\theta & \cos\theta \end{pmatrix}}_{\mathbb{R}}\begin{pmatrix} \chi_1 \\ \chi_2^\dagger \end{pmatrix}. \tag{A17}$$

From Eq. (A17), we get $\chi_1^0 = \mathbb{R}_{11}\chi_1 + \mathbb{R}_{12}\chi_2^\dagger$ and $(\chi_2^0)^\dagger = \mathbb{R}_{21}\chi_1 + \mathbb{R}_{22}\chi_2^\dagger$, and the Lagrangian can be expressed in terms of these new physical bases, χ_1 and χ_2, as

$$\mathcal{L}^{\rm phy} = \mathcal{L}_{\rm SM} + \mathcal{L}^{\rm kin}_{\chi_1\chi_2} + \mathcal{L}^{\rm mass}(\chi_1,\chi_2) + \mathcal{L}^{\rm int}(\chi_1,\chi_2,H), \tag{A18}$$

where

$$\mathcal{L}^{\rm kin}_{\chi_1\chi_2} = (\partial_\mu\chi_1)^\dagger(\partial^\mu\chi_1) + (\partial_\mu\chi_2)^\dagger(\partial^\mu\chi_2), \tag{A19}$$

$$\mathcal{L}^{\rm mass}_{\chi_1\chi_2} = m^2_{\chi_1}\chi_1^\dagger\chi_1 + m^2_{\chi_2}\chi_2^\dagger\chi_2, \tag{A20}$$

$$\begin{aligned}\mathcal{L}^{\rm int}(\chi_1,\chi_2,H) = {}& \lambda_{\chi_1}|\chi_1|^4 + \lambda_{\chi_2}|\chi_2|^4 + \lambda_{1H}|\chi_1|^2(\mathrm{H}^\dagger\mathrm{H} - v^2/2) + \lambda_{2H}|\chi_2|^2(\mathrm{H}^\dagger\mathrm{H} - v^2/2) + \lambda_{12}|\chi_1|^2|\chi_2|^2 \\ & + \frac{1}{2}\lambda_{12H}(\chi_1\chi_2 + \text{H.c.})(\mathrm{H}^\dagger\mathrm{H} - v^2/2) + \frac{1}{2}\lambda'_{12}[(\chi_1\chi_2)^2 + \text{H.c.}] + \frac{1}{2}[\lambda_3\chi_1\chi_2|\chi_1|^2 + \lambda_4\chi_1\chi_2|\chi_2|^2 + \text{H.c.}] \\ & + \frac{1}{2}[\mu_1\chi_2^2\chi_1^* + \mu_2\chi_1^2\chi_2^* + \mu_3\chi_1^3 + \mu_4\chi_2^3 + \text{H.c.}],\end{aligned} \tag{A21}$$

with

$$\begin{aligned}\lambda_{\chi_1} = {}& 2\kappa_+^3\kappa_-\sin\theta\cos^3\theta(-2\lambda^0_{\chi_1} + 2\lambda^0_{\chi_2} - \lambda^0_3 + \lambda^0_4) + 2\kappa_+\kappa_-^3\sin^3\theta\cos\theta(-2\lambda^0_{\chi_1} + 2\lambda^0_{\chi_2} + \lambda^0_3 - \lambda^0_4) \\ & + \kappa_-^4\sin^4\theta(\lambda^0_{\chi_1} + \lambda^0_{\chi_2} - \lambda^0_3 - \lambda^0_4 + \lambda^0_{12} + \lambda^{0'}_{12}) + \kappa_+^4\cos^4\theta(\lambda^0_{\chi_1} + \lambda^0_{\chi_2} + \lambda^0_3 + \lambda^0_4 + \lambda^0_{12} + \lambda^{0'}_{12}) \\ & - 2\kappa_+^2\kappa_-^2\sin^2\theta\cos^2\theta(-3(\lambda^0_{\chi_1} + \lambda^0_{\chi_2}) + \lambda^0_{12} + \lambda^{0'}_{12}),\end{aligned} \tag{A22}$$

$$\begin{aligned}\lambda_{\chi_2} = {}& 2\kappa_+\kappa_-^3\sin\theta\cos^3\theta(2\lambda^0_{\chi_1} - 2\lambda^0_{\chi_2} - \lambda^0_3 + \lambda^0_4) + 2\kappa_+^3\kappa_-\sin^3\theta\cos\theta(2\lambda^0_{\chi_1} - 2\lambda^0_{\chi_2} + \lambda^0_3 - \lambda^0_4) \\ & + \kappa_+^4\sin^4\theta(\lambda^0_{\chi_1} + \lambda^0_{\chi_2} + \lambda^0_3 + \lambda^0_4 + \lambda^0_{12} + \lambda^{0'}_{12}) + \kappa_-^4\cos^4\theta(\lambda^0_{\chi_1} + \lambda^0_{\chi_2} - \lambda^0_3 - \lambda^0_4 + \lambda^0_{12} + \lambda^{0'}_{12}) \\ & - 2\kappa_+^2\kappa_-^2\sin^2\theta\cos^2\theta(-3(\lambda^0_{\chi_1} + \lambda^0_{\chi_2}) + \lambda^0_{12} + \lambda^{0'}_{12}),\end{aligned} \tag{A23}$$

$$\begin{aligned}\frac{1}{2}\lambda_3 = {}& -\frac{1}{2}\kappa_+^3\kappa_-(\cos(2\theta) + \cos(4\theta))(2\lambda^0_{\chi_1} - 2\lambda^0_{\chi_2} + \lambda^0_3 - \lambda^0_4) + \kappa_+\kappa_-^3\sin^2\theta(2\cos(2\theta) + 1)(-2\lambda^0_{\chi_1} + 2\lambda^0_{\chi_2} + \lambda^0_3 - \lambda^0_4) \\ & - \frac{1}{2}\kappa_+^2\kappa_-^2\sin(4\theta)(-3(\lambda^0_{\chi_1} + \lambda^0_{\chi_2}) + \lambda^0_{12} + \lambda^{0'}_{12}) - 2\kappa_+^4\sin\theta\cos^3(\theta)(\lambda^0_{\chi_1} + \lambda^0_{\chi_2} + \lambda^0_3 + \lambda^0_4 + \lambda^0_{12} + \lambda^{0'}_{12}) \\ & - 2\kappa_-^4\sin^3\theta\cos\theta(-\lambda^0_{\chi_1} - \lambda^0_{\chi_2} + \lambda^0_3 + \lambda^0_4 - \lambda^0_{12} - \lambda^{0'}_{12}),\end{aligned} \tag{A24}$$

$$\begin{aligned}\frac{1}{2}\lambda_4 = {}& \frac{1}{2}\kappa_+\kappa_-^3(\cos(2\theta) + \cos(4\theta))(-2\lambda^0_{\chi_1} + 2\lambda^0_{\chi_2} + \lambda^0_3 - \lambda^0_4) - \kappa_+^3\kappa_-\sin^2\theta(2\cos(2\theta) + 1)(2\lambda^0_{\chi_1} - 2\lambda^0_{\chi_2} + \lambda^0_3 - \lambda^0_4) \\ & + \frac{1}{2}\kappa_+^2\kappa_-^2\sin(4\theta)(-3(\lambda^0_{\chi_1} + \lambda^0_{\chi_2}) + \lambda^0_{12} + \lambda^{0'}_{12}) - 2\kappa_-^4\sin\theta\cos^3\theta(-\lambda^0_{\chi_1} - \lambda^0_{\chi_2} + \lambda^0_3 + \lambda^0_4 - \lambda^0_{12} - \lambda^{0'}_{12}) \\ & - 2\kappa_+^4\sin^3\theta\cos\theta(\lambda^0_{\chi_1} + \lambda^0_{\chi_2} + \lambda^0_3 + \lambda^0_4 + \lambda^0_{12} + \lambda^{0'}_{12}),\end{aligned} \tag{A25}$$

$$\begin{aligned}\lambda_{12} = {}& \kappa_+\kappa_-^3\sin(4\theta)(-2\lambda^0_{\chi_1} + 2\lambda^0_{\chi_2} + \lambda^0_3 - \lambda^0_4) + \kappa_+^3\kappa_-\sin(4\theta)(2\lambda^0_{\chi_1} - 2\lambda^0_{\chi_2} + \lambda^0_3 - \lambda^0_4) \\ & + \kappa_-^4(-\sin^2(2\theta))(-\lambda^0_{\chi_1} - \lambda^0_{\chi_2} + \lambda^0_3 + \lambda^0_4 - \lambda^0_{12} - \lambda^{0'}_{12}) + \kappa_+^4\sin^2(2\theta)(\lambda^0_{\chi_1} + \lambda^0_{\chi_2} + \lambda^0_3 + \lambda^0_4 + \lambda^0_{12} + \lambda^{0'}_{12}) \\ & - \kappa_+^2\kappa_-^2(-(3\cos(4\theta) + 1)(\lambda^0_{\chi_1} + \lambda^0_{\chi_2}) + \lambda^0_{12}(\cos(4\theta) - 1) + (\cos(4\theta) + 3)\lambda^{0'}_{12}),\end{aligned} \tag{A26}$$

$$\begin{aligned}\frac{1}{2}\lambda'_{12} = {}& \frac{1}{8}(2\kappa_+\kappa_-^3\sin(4\theta)(-2\lambda^0_{\chi_1} + 2\lambda^0_{\chi_2} + \lambda^0_3 - \lambda^0_4) + 2\kappa_+^3\kappa_-\sin(4\theta)(2\lambda^0_{\chi_1} - 2\lambda^0_{\chi_2} + \lambda^0_3 - \lambda^0_4) \\ & + 2\kappa_+^4\sin^2(2\theta)(\lambda^0_{\chi_1} + \lambda^0_{\chi_2} + \lambda^0_3 + \lambda^0_4 + \lambda^0_{12} + \lambda^{0'}_{12}) + \kappa_-^4(\cos(4\theta) - 1)(-\lambda^0_{\chi_1} - \lambda^0_{\chi_2} + \lambda^0_3 + \lambda^0_4 - \lambda^0_{12} - \lambda^{0'}_{12}) \\ & - 2\kappa_+^2\kappa_-^2(-(3\cos(4\theta) + 1)(\lambda^0_{\chi_1} + \lambda^0_{\chi_2}) + \lambda^0_{12}(\cos(4\theta) + 3) + (\cos(4\theta) - 5)\lambda^{0'}_{12})),\end{aligned} \tag{A27}$$

$$\lambda_{1H} = \kappa_+^2\cos^2\theta(\lambda^0_{1H} + \lambda^0_{2H} + 2\lambda^0_{12H}) + \kappa_-\sin\theta(\kappa_-\sin\theta(\lambda^0_{1H} + \lambda^0_{2H} - 2\lambda^0_{12H}) + 2\kappa_+\cos\theta(\lambda^0_{2H} - \lambda^0_{1H})), \tag{A28}$$

$$\lambda_{2H} = \kappa_-^2\cos^2\theta(\lambda^0_{1H} + \lambda^0_{2H} - 2\lambda^0_{12H}) + \kappa_+\sin\theta(\kappa_+\sin\theta(\lambda^0_{1H} + \lambda^0_{2H} + 2\lambda^0_{12H}) + 2\kappa_-\cos\theta(\lambda^0_{1H} - \lambda^0_{2H})), \tag{A29}$$

$$\frac{1}{2}\lambda_{12H} = -\kappa_-\kappa_+\sin^2\theta(\lambda^0_{1H} - \lambda^0_{2H}) + \kappa_-\kappa_+\cos^2\theta(\lambda^0_{2H} - \lambda^0_{1H}) + (\kappa_- - \kappa_+)(\kappa_- + \kappa_+)\sin\theta\cos\theta(\lambda^0_{1H} + \lambda^0_{2H}) + (\kappa_-^2 + \kappa_+^2)(-\sin(2\theta))\lambda^0_{12H}, \tag{A30}$$

$$\frac{1}{2}\mu_1 = \frac{1}{2}\left(\frac{1}{4}\kappa_+^2\kappa_-(\mu^0_1 - \mu^0_2 - 3\mu^0_3 + 3\mu^0_4)\right)(\sin\theta - 3\sin(3\theta)) - \frac{1}{4}\kappa_+\kappa_-^2(\mu^0_1 + \mu^0_2 - 3(\mu^0_3 + \mu^0_4))(\cos\theta + 3\cos(3\theta)) - 3\kappa_-^3(\mu^0_1 - \mu^0_2 + \mu^0_3 - \mu^0_4)\sin\theta\cos^2\theta + 3\kappa_+^3(\mu^0_1 + \mu^0_2 + \mu^0_3 + \mu^0_4)\sin^2\theta\cos\theta), \tag{A31}$$

$$\frac{1}{2}\mu_2 = \frac{1}{2}\left(\frac{1}{4}\kappa_+\kappa_-^2(\mu^0_1 + \mu^0_2 - 3(\mu^0_3 + \mu^0_4))(\sin\theta - 3\sin(3\theta)) + \frac{1}{4}\kappa_+^2\kappa_-(\mu^0_1 - \mu^0_2 - 3\mu^0_3 + 3\mu^0_4)(\cos\theta + 3\cos(3\theta)) - 3\kappa_+^3(\mu^0_1 + \mu^0_2 + \mu^0_3 + \mu^0_4)\sin\theta\cos^2\theta - 3\kappa_-^3(\mu^0_1 - \mu^0_2 + \mu^0_3 - \mu^0_4)\sin^2\theta\cos\theta\right), \tag{A32}$$

$$\frac{1}{2}\mu_3 = \frac{1}{2}(-(\kappa_-^2\sin^2\theta - \kappa_+^2\cos^2\theta)(\kappa_-(\mu^0_1 - \mu^0_2)\sin\theta + \kappa_+(\mu^0_1 + \mu^0_2)\cos\theta) + \mu^0_3(-(\kappa_-\sin\theta - \kappa_+\cos\theta)^3) + \mu^0_4(\kappa_-\sin\theta + \kappa_+\cos\theta)^3), \tag{A33}$$

$$\frac{1}{2}\mu_4 = \frac{1}{2}(\mu^0_3(-(\kappa_+\sin\theta + \kappa_-\cos\theta)^3) + \mu^0_4(\kappa_-\cos\theta - \kappa_+\sin\theta)^3 + (\kappa_-\cos\theta - \kappa_+\sin\theta)(\kappa_+\sin\theta + \kappa_-\cos\theta)(\kappa_+(\mu^0_1 + \mu^0_2)\sin\theta - \kappa_-(\mu^0_1 - \mu^0_2)\cos\theta)). \tag{A34}$$

APPENDIX B: HEAVY DM STABILITY CRITERIA FROM TWO- AND THREE-BODY DECAYS

The two-body decay width in the rest frame of the decaying particle (A_0), $A_0(m_0) \to A_1(m_1)A_2(m_2)$ [Fig. 9(a)] is given by [109]

$$\Gamma_{A_0\to A_1A_2} = \frac{1}{64\pi^2 m_0}\sqrt{\left[1 - \left(\frac{m_1 + m_2}{m_0}\right)^2\right]\left[1 - \left(\frac{m_1 - m_2}{m_0}\right)^2\right]}\int \overline{|\mathcal{M}|^2}d\Omega. \tag{B1}$$

Let us consider a process like $A_0(m_0) \to A_1(m_1)A_2(m_2)A_3(m_3)$, where three particles can be produced by three different kinds of processes as shown in Fig. 9. The three-body decay width in the rest frame of the decaying particle (A_0) is given by [110]

$$\Gamma_{A_0\to A_1A_2..A_n} = S_k\frac{1}{2m_0}\left(\prod_{i=1}^{n}\int\frac{d^3p_i'}{(2\pi)^3 2E_i'}\right)(2\pi)^4\delta^4\left(p - \sum_{i=1}^{n}p_i'\right)\overline{|\mathcal{M}|^2}_{A_0\to A_1A_2..A_n}. \tag{B2}$$

$S_k = 1/k!$ is the corresponding symmetry factor, with k the number of identical final state particles. In the CM reference frame, the expression for the three body decay width [111],

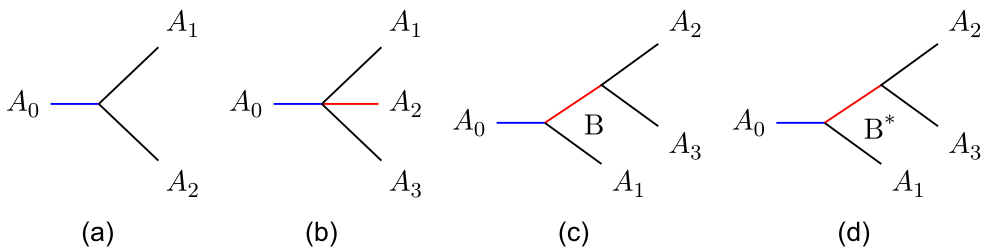


FIG. 9. Panel (a) shows the two-body decay when $m_0 > \sum_{i=1}^{2} m_i$. The rest of the panels show the possible three-body decay: four-point (b), off-shell B (c), on-shell B (d).

$$\Gamma_{A_0\to A_1A_2A_3} = S_k \frac{1}{(2\pi)^3}\frac{1}{32m_0^3}\int dm_{12}^2 \int dm_{23}^2 \overline{|\mathcal{M}|^2}_{A_0\to A_1A_2A_3}, \tag{B3}$$

where

$$m_{23}^2|_{\max} = (E_2^* + E_3^*)^2 - \left(\sqrt{E_2^{*2} - m_2^2} - \sqrt{E_3^{*2} - m_3^2}\right)^2, \tag{B4}$$

$$m_{23}^2|_{\min} = (E_2^* + E_3^*)^2 - \left(\sqrt{E_2^{*2} - m_2^2} + \sqrt{E_3^{*2} - m_3^2}\right)^2, \tag{B5}$$

$$m_{12}^2|_{\max} = (m_0 - m_3)^2 \quad \text{and} \quad m_{12}^2|_{\min} = (m_1 + m_2)^2, \tag{B6}$$

$$E_2^* = (m_{12}^2 - m_1^2 + m_2^2)/2m_{12} \quad \text{and}$$
$$E_3^* = (m_0^2 - m_{12}^2 - m_3^2)/2m_{12}. \tag{B7}$$

1. First alternative way

$$\Gamma_{A_0\to A_1A_2A_3} = \frac{1}{(2\pi)^3}\frac{1}{8m_0}\int_{E_1^{\min}}^{E_1^{\max}} dE_1 \int_{E_2^{\min}}^{E_2^{\max}} dE_2 \overline{|\mathcal{M}|^2}_{A_0\to A_1A_2A_3}, \tag{B8}$$

where the minimum and maximum energy of the particles in the CM frame are [39,111]

$$E_2^{\min} = \frac{1}{2m_{23}^2}\left[(m_0 - E_1)m_{23}^2 - \sqrt{(E_1^2 - m_1^2)\lambda(m_{23}^2, m_2^2, m_3^2)}\right], \tag{B9}$$

$$E_2^{\max} = \frac{1}{2m_{23}^2}\left[(m_0 - E_1)m_{23}^2 + \sqrt{(E_1^2 - m_1^2)\lambda(m_{23}^2, m_2^2, m_3^2)}\right], \tag{B10}$$

with

$$m_{23}^2 = m_0^2 + m_1^2 - 2m_0E_1, \tag{B11}$$

$$\lambda(a,b,c) \equiv a^2 + b^2 + c^2 - 2ab - 2bc - 2ca, \tag{B12}$$

$$E_1^{\min} = m_1, \qquad E_1^{\max} = \frac{1}{2m_0}(m_0^2 + m_1^2 - 4m_2^2), \tag{B13}$$

and λ is the Källén function.

2. Second alternative way

Here [111,112],

$$d\Gamma_{A_0\to A_1A_2A_3} = \frac{1}{64m_0^3}\frac{1}{(2\pi)^3}\frac{\sqrt{\lambda(m_0^2, m_1^2, q^2)\lambda(q^2, m_2^2, m_3^2)}}{q^2} \times dq^2 d\cos\theta^* |\mathcal{M}|^2_{A_0\to A_1A_2A_3} \tag{B14}$$

where $q = p_0 - p_1$, $q_{\min}^2 = (m_2 + m_3)^2$, $q_{\max}^2 = (m_0 - m_1)^2$.

3. Tree- and loop-level decay of the heavy DM with $\mathcal{Z}_2$ symmetry

The presence of the Higgs portal interaction for ϕ_1 and ϕ_2, as described in Eq. (3.2), allows the heavier particle to decay to the lighter particle along with a Higgs boson. The Higgs, whether on-shell or off-shell, can substantially decay into a pair of photons or gluons. The decay of the heavier particle in a nondegenerate scenario imposes stringent constraints on the associated couplings, implying that the mass hierarchy is not limited to just the Higgs mass. Figure 10 illustrates the decay of the heavier particle into the lighter one plus an on-shell Higgs. The decay width involving an off-shell Higgs, which decays into light fermions or massless bosons, is significantly suppressed, so we consider only the on-shell Higgs in the total decay width calculation (tree-level + loop correction) to derive stringent limits on the couplings associated with the $\phi_2 \to \phi_1 h$ decay. We do not delve into the details of the complicated loop calculation; instead, we provide an approximate estimate of the coupling required to stabilize the heavier DM particle. The vertex factor corresponding to the tree-level decay process, shown in Fig. 10(a), is $\lambda_{\phi_1\phi_2 H} v$. We aim to determine the stringent limit on this coupling such that the decay time of the heavier particle, τ_{ϕ_2}, exceeds the

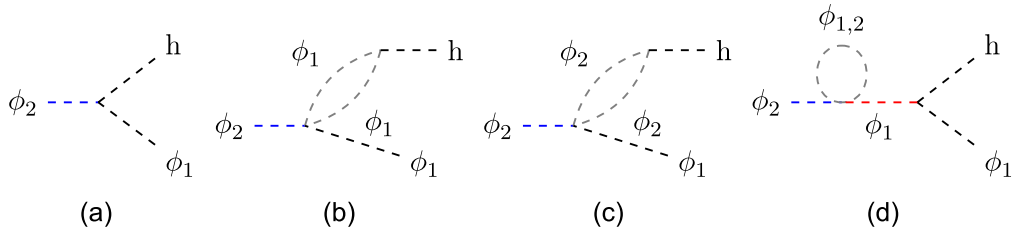


FIG. 10. Panels (a)–(d) correspond to the tree- and one-loop level decays of ϕ_2 to ϕ_1 plus on-shell Higgs under the assumption $m_{\phi_2} > m_{\phi_1}$, respectively. However, the Higgs off-shell decay to a diphoton or digluon would always be there for two nondegenerate DM components.

TABLE VI. A few examples bound on the parameters to stabilize ϕ_2 DM, which is also odd under $\mathcal{Z}_2$. Other parameters appearing in the decay width are taken as $\lambda_{1H} = 1$. More importantly, the lifetime of the decaying DM has to be greater than the age of our Universe, 6.4×10^{41} GeV^{-1}.

Decay channel	m_{ϕ_2} [GeV]	m_{ϕ_1} [GeV]	λ_{12H}	λ_{112}	Lifetime [GeV^{-1}]
$\phi_2 \to \phi_1 h$	200	70	10^{-21}	⋯	7.77×10^{41}
$\phi_2 \to \phi_1$ SM SM	200	70	10^{-21}	10^{-19}	1.30×10^{42}
$\phi_2 \to \phi_1$ SM SM	200	110	10^{-21}	10^{-19}	2.91×10^{47}
$\phi_2 \to \phi_1$ All	200	70	10^{-21}	10^{-16}	7.77×10^{41}
$\phi_2 \to \phi_1$ All	200	110	10^{-21}	10^{-16}	5.43×10^{42}

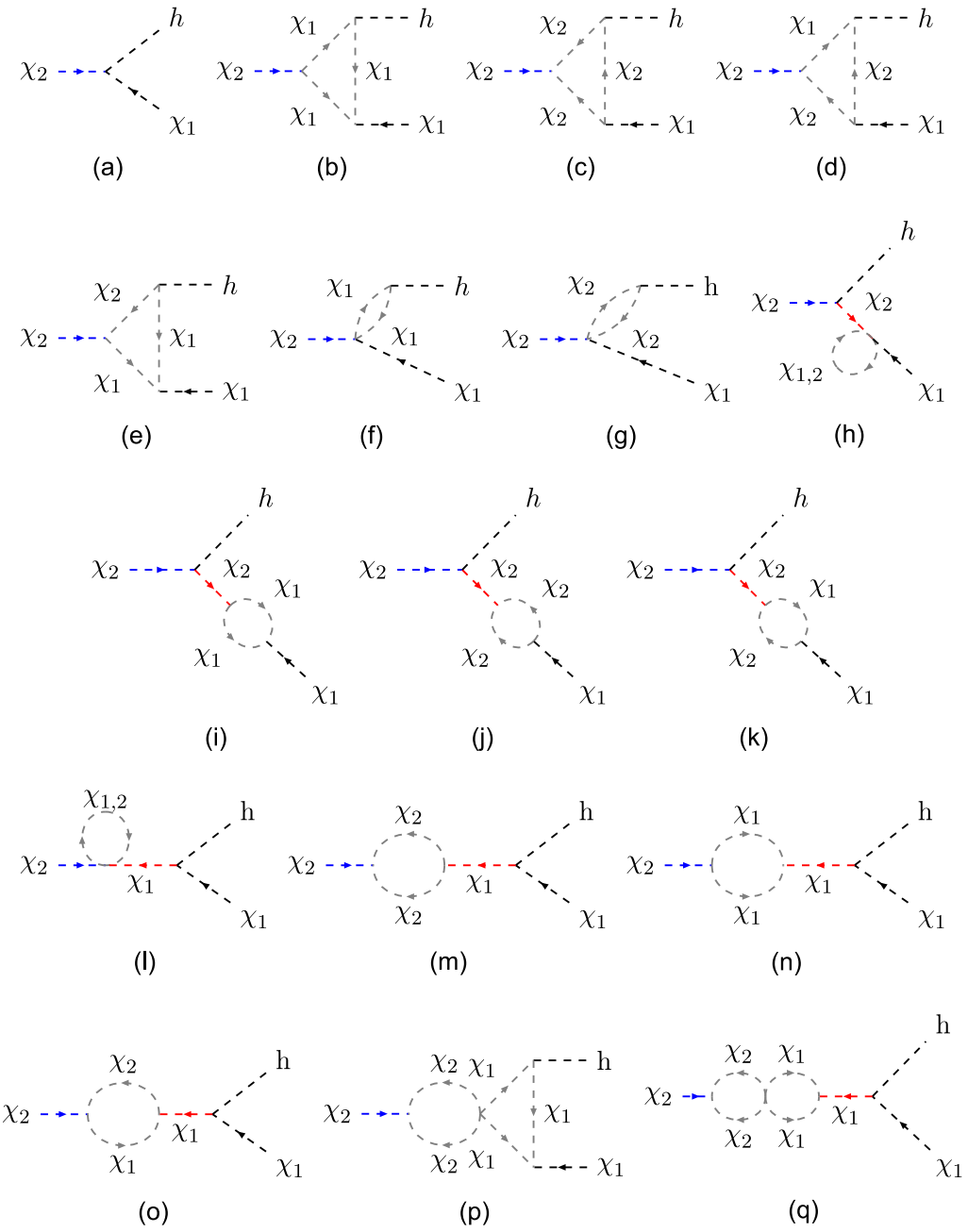


FIG. 11. Panel (a) is the Feynman diagram corresponding to the tree-level decay: $\chi_2 \to \chi_1 h$. After ignoring the diagrams involving the $h\chi_1\chi_2$ vertex, the remaining Feynman diagrams, panels (b) to (o), represent the one-loop mediated decay after the appropriate choice (see Table III) of sacrificing coupling associated with the one-loop decay, and there are still possible two-loop decay processes [(p) and (q)].

TABLE VII. The bound on particular parameters to have the lifetime of the $\mathcal{Z}_3$ charged DM greater than the age of the Universe, 6.4×10^{41} GeV^{-1}. The other parameter values that will appear in the decay width of the DM are taken as $\mu_1 = \mu_3 = \mu_4 = 2m_{\chi_1}$, $\lambda_{1H} = \lambda_{12} = \lambda'_{12} = \lambda_4 = 1$.

Decay channel	m_{χ_2} [GeV]	m_{χ_1} [GeV]	μ_2 [GeV]	λ_{12H}	λ_3	Lifetime [GeV^{-1}]
$\chi_2 \to \chi_1 h$	200	70	10^{-17}	10^{-21}	10^{-19}	1.70×10^{42}
$\chi_2 \to \chi_1 h$	200	70	10^{-19}	10^{-21}	10^{-19}	1.58×10^{42}
$\chi_2 \to \chi_1 h$	200	50	10^{-17}	10^{-21}	10^{-19}	6.40×10^{42}
$\chi_2 \to \chi_1$ SM SM	200	70	10^{-15}	10^{-21}	10^{-15}	6.50×10^{42}
$\chi_2 \to \chi_1$ SM SM	200	110	10^{-15}	10^{-21}	10^{-15}	1.74×10^{48}
$\chi_2 \to \chi_1$ All	200	110	10^{-15}	10^{-21}	10^{-15}	1.74×10^{48}
$\chi_2 \to \chi_1$ All	200	70	10^{-15}	10^{-21}	10^{-15}	6.50×10^{42}

age of the Universe: $\tau_{\rm univ} = 6.4 \times 10^{41}$ GeV^{-1}. The decay time for the tree-level $\phi_2 \to \phi_1 h$ process is

$$\tau_{\phi_2}^{-1} = \frac{\lambda_{\phi_1\phi_2 H}^2 v^2}{16\pi m_{\phi_2}} \sqrt{\left[1 - \left(\frac{m_{\phi_1} + m_h}{m_{\phi_2}}\right)^2\right]\left[1 - \left(\frac{m_{\phi_1} - m_h}{m_{\phi_2}}\right)^2\right]}. \tag{B15}$$

The tree-level decay shown in Fig. 10(a) indicates that a coupling of $\lambda_{\phi_1\phi_2 H} \lesssim 10^{-22}$ is sufficient to ensure that τ_{ϕ_2} exceeds the age of the Universe, $\tau_{\rm univ}$. At the next order, a one-loop decay is also possible. However, we disregard diagrams involving the $h\phi_1\phi_2$ vertex in one-loop decay, as these would be suppressed compared to the tree-level decay. The relevant decay diagrams are shown in Figs. 10(b)–10(d). Stringent limits on the λ_{112} and λ_{122} couplings are necessary to stabilize the heavier particle. These couplings are expected to be $\gtrsim \lambda_{\phi_1\phi_2 H}$ due to the loop suppression factor of $1/(16\pi^2)$. However, a proper loop calculation is required to determine the upper limit accurately. Ideally, the total decay width of ϕ_2 should include contributions from both the tree-level and all relevant one-loop decays. However, the presence of UV divergences in the loop diagrams adds complexity to this process, which we have not explored in detail here. Instead, we focus on finding the appropriate combination of m_{ϕ_1}, m_{ϕ_2}, $\lambda_{\phi_1\phi_2 H}$, λ_{112}, and λ_{122} that stabilizes ϕ_2, ensuring that $\tau_{\phi_2} > \tau_{\rm univ}$, while keeping the other parameters within a weak ordering regime.

4. Tree- and loop-level decay of the heavy DM with $\mathcal{Z}_3$ symmetry

Similar to the case with $\mathcal{Z}_2$ symmetry, there are decay channels for the heavier DM particle under $\mathcal{Z}_3$ symmetry as well. The interactions between the DM particles and visible sectors, as shown in Eq. (3.2), give rise to tree-level, one-loop, and two-loop decay processes. Let us analyze these decay processes step by step, assuming $m_{\chi_2} > m_{\chi_1}$. However, the decay constraints are equally applicable to the opposite mass hierarchy.

(1) The tree-level decay process $\chi_2 \to \chi_1^* + h$ [see Fig. 11(a)] is mediated by the coupling λ_{12H}. According to Appendix (B15), to ensure $\tau_{\chi_2} > \tau_{\rm univ}$ in the presence of this tree-level decay, we require $\lambda_{12H} \lesssim 4 \times 10^{-22}$.

(2) If we ignore the diagrams involving the λ_{12H} coupling, we obtain one-loop decay diagrams, as shown in Figs. 11(b) to 11(o). The associated interaction terms and their corresponding couplings, whose small

TABLE VIII. Diagramwise operators contributing to the process of the decay of the LLP dark matter component for the mass hierarchy $m_{\chi_2} > m_{\chi_1}$. The corresponding interactions marked by the symbols (†, ‡, ♣, ♠, △, ◇, and ∘) are sacrificed in different scenarios corresponding to Table III.

Diagram	Contributing operators
	Tree-level
Fig. 11(a)	$\chi_1\chi_2 H^\dagger H$
	One-loop
Fig. 11(b)	$\lvert\chi_1\rvert^2\lvert H\rvert^2$, $^\dagger\chi_1^2\chi_2^*$, $^\diamond\chi_1^3$
Fig. 11(c)	$\lvert\chi_2\rvert^2\lvert H\rvert^2$, $^\spadesuit\chi_1^*\chi_2^2$, $^\clubsuit\chi_2^3$
Fig. 11(d)	$\chi_1\chi_2 H^\dagger H$, $\chi_1^*\chi_2^2$, $\chi_1\chi_2^{*2}$
Fig. 11(e)	$\chi_1\chi_2 H^\dagger H$, $^\spadesuit\chi_1^*\chi_2^2$, $^\diamond\chi_1^3$
Fig. 11(f)	$\lvert\chi_1\rvert^2\lvert H\rvert^2$, $^\triangle\lvert\chi_1\rvert^2\chi_1\chi_2$
Fig. 11(g)	$\lvert\chi_2\rvert^2\lvert H\rvert^2$, $^\ddagger\chi_1\chi_2\lvert\chi_2\rvert^2$
Fig. 11(h)	$\lvert\chi_2\rvert^2\lvert H\rvert^2$, $^\triangle\lvert\chi_1\rvert^2\chi_1\chi_2/^\ddagger\chi_1\chi_2\lvert\chi_2\rvert^2$
	One-loop (contd.)
Fig. 11(i)	$\lvert\chi_2\rvert^2\lvert H\rvert^2$, $^\dagger\chi_1^2\chi_2^*$, $^\diamond\chi_1^3$
Fig. 11(j)	$\lvert\chi_2\rvert^2\lvert H\rvert^2$, $^\spadesuit\chi_1^*\chi_2^2$, $^\clubsuit\chi_2^3$
Fig. 11(k)	$\lvert\chi_2\rvert^2\lvert H\rvert^2$, $^\spadesuit\chi_1^*\chi_2^2$, $^\dagger\chi_1^2\chi_2^*$
Fig. 11(l)	$\lvert\chi_1\rvert^2\lvert H\rvert^2$, $^\dagger\chi_1\chi_2\lvert\chi_2\rvert^2/^\triangle\lvert\chi_1\rvert^2\chi_1\chi_2$
Fig. 11(m)	$\lvert\chi_1\rvert^2\lvert H\rvert^2$, $^\spadesuit\chi_1^*\chi_2^2$, $^\clubsuit\chi_2^3$
Fig. 11(n)	$\lvert\chi_1\rvert^2\lvert H\rvert^2$, $^\dagger\chi_1^2\chi_2^*$, $^\diamond\chi_1^3$
Fig. 11(o)	$\lvert\chi_1\rvert^2\lvert H\rvert^2$, $^\spadesuit\chi_1^*\chi_2^2$, $^\dagger\chi_1^2\chi_2^*$
	Two-loop
Fig. 11(p)	$\lvert\chi_1\rvert^2\lvert H\rvert^2$, $^\circ\chi_1^2\chi_2^2$, $^\diamond\chi_1^3$, $^\clubsuit\chi_2^3$
Fig. 11(q)	$\lvert\chi_1^2\rvert\lvert H\rvert^2$, $^\circ\chi_1^2\chi_2^2$, $^\diamond\chi_1^3$, $^\clubsuit\chi_2^3$

values contribute to the stability of χ_2, present various scenarios, as summarized in Table III.

(3) In specific cases, there may also be two-loop decay processes, such as those depicted in Figs. 11(p) and 11(q). To stabilize χ_2, the couplings associated with these decays must be minimized, although the constraints will be less stringent than the one-loop limits due to the suppression factor $(16\pi^2)^{-2}$.

Although we have imposed constraints on the couplings associated with each decay process, the total decay width is the sum of contributions from tree-level, one-loop, and two-loop processes. Calculating the total decay width is a highly complicated task, and while the precise limits on the couplings may shift slightly with a more accurate computation, the overall phenomenology remains unchanged.

In Tables III and IV, we present six different scenarios arising from a $\mathcal{Z}_3$ symmetry, categorized based on the choices of q_1 and q_2. Scenarios A, B, and C correspond to the case where $q_1 \neq q_2$ and $q_1 + q_2 = N(= 3)$, while scenarios D, E, and F represent the case where $q_1 = q_2$ but $q_1 + q_2 \neq N$. In each scenario, certain operators or interaction strengths must be suppressed to obtain a stable dark matter candidate, one being absolutely stable and the other an LLP. The corresponding decay diagrams at the tree-, one-loop, and two-loop levels for the mass hierarchy $m_{\chi_2} > m_{\chi_1}$ are shown in Fig. 11. For the opposite hierarchy, $m_{\chi_1} > m_{\chi_2}$, similar/inverted diagrams contribute to the decay of χ_1, and the required operator suppression would remain the same.

Table VIII lists all relevant couplings associated with the decay diagrams in Fig. 11, organized by loop order. We have highlighted, using color, the specific operators sacrificed in each scenario. The tree-level diagrams vanish if the coupling $\chi_1\chi_2 H^\dagger H$ is negligible. Suppressing this operator allows us to further reduce one-loop contributions by taking couplings like $\chi_1^*\chi_2^2$, $\chi_1^2\chi_2^*$, χ_1^3, and χ_2^3 to be small. Additionally, making the $\chi_1^2\chi_2^2$ coupling small suppresses the two-loop decay channels, which helps ensure that χ_2 behaves as an LLP. Once the two-loop decay is sufficiently suppressed, higher-loop decays (three-loop and beyond) are automatically negligible, thereby protecting the LLP's longevity.

APPENDIX C: UNITARITY BOUNDS ON THE MODEL PARAMETERS

In order to study the tree-level unitarity bounds on the quartic couplings of our model at high energies, we consider the generic structure of $2 \to 2$ scattering amplitudes. These amplitudes can be expanded in terms of Legendre polynomials as [113]

$$\mathcal{M}^{2\to 2} = 16\pi \sum_{l=0}^{\infty} a_l (2l+1) P_l(\cos\theta), \tag{C1}$$

where θ is the scattering angle and $P_l(\cos\theta)$ denotes the Legendre polynomial of order l. In the high-energy limit, the dominant contribution comes from the s wave ($l = 0$), with the partial amplitude a_0 governing the leading behavior of the process. The unitarity condition then requires

$$|\mathrm{Re}(a_0)| \leq \frac{1}{2}. \tag{C2}$$

The above constraint can be equivalently expressed as a bound on the full scattering amplitude $\mathcal{M}$ [90,114,115]:

$$|\mathcal{M}| \leq 8\pi. \tag{C3}$$

When multiple $2 \to 2$ processes are possible, one needs to construct an S-scattering matrix $\mathcal{M}^{2\to 2}_{i,j} = \mathcal{M}_{i\to j}$ by taking into account all possible two-particle states. In the high-energy limit, the SM Higgs doublet is expressed as $H = (G^+ \frac{h+iG^0}{\sqrt{2}})^T$, and the interaction Lagrangian in Eqs. (4.1) and (4.2) gives rise to 22 two-particle neutral states:

$$\begin{aligned}\Big\{ &\frac{hh}{\sqrt{2}}, \frac{G^0G^0}{\sqrt{2}}, G^+G^-, hG^0, \\ &h\chi_i, h\chi_i^*, G^0\chi_i, G^0\chi_i^*, \\ &\frac{\chi_i\chi_i}{\sqrt{2}}, \frac{\chi_i^*\chi_i^*}{\sqrt{2}}, \chi_i\chi_i^*, \chi_1\chi_2, \chi_1^*\chi_2^*, \chi_1\chi_2^*, \chi_1^*\chi_2 \Big\},\end{aligned} \tag{C4}$$

where $i = 1, 2$. The single charge six two-particle state is

$$\sum_{i=1,2} \{hG^\pm, G^0G^\pm, \chi_i G^\pm, \chi_i^* G^\pm\}, \tag{C5}$$

and only one double charge two-particle state is

$$\frac{G^\pm G^\pm}{\sqrt{2}}. \tag{C6}$$

Therefore, the scattering amplitude matrix $(\mathcal{M})$ can be expressed in block-diagonal form by decomposing it into the neutral (NC), singly charged (SC), and double charged states as [116]

$$\mathcal{M} = \begin{pmatrix} \mathcal{M}^{\mathrm{NC}}_{22\times 22} & 0 & 0 \\ 0 & \mathcal{M}^{\mathrm{SC}}_{6\times 6} & 0 \\ 0 & 0 & \mathcal{M}^{\mathrm{DC}}_{1\times 1} \end{pmatrix}, \tag{C7}$$

with the submatrices given by

$$\mathcal{M}^{\rm NC}_{22\times 22}=\begin{pmatrix}\mathcal{M}^{\rm HH}_{{\rm HH}_{4\times4}} & \mathcal{M}^{\rm HH}_{{\rm H}\chi_{4\times8}} & \mathcal{M}^{\rm HH}_{\chi\chi_{4\times10}}\\ \mathcal{M}^{\rm H\chi}_{{\rm HH}_{8\times4}} & \mathcal{M}^{\rm H\chi}_{{\rm H}\chi_{8\times8}} & \mathcal{M}^{\rm H\chi}_{\chi\chi_{8\times10}}\\ \mathcal{M}^{\chi\chi}_{{\rm HH}_{10\times4}} & \mathcal{M}^{\chi\chi}_{{\rm H}\chi_{10\times8}} & \mathcal{M}^{\chi\chi}_{\chi\chi_{10\times10}}\end{pmatrix}=\begin{pmatrix}\mathcal{M}^{\rm HH}_{{\rm HH}_{4\times4}} & 0_{4\times8} & \mathcal{M}^{\rm HH}_{\chi\chi_{4\times10}}\\ 0_{8\times4} & \mathcal{M}^{\rm H\chi}_{{\rm H}\chi_{8\times8}} & 0_{8\times10}\\ \mathcal{M}^{\chi\chi}_{{\rm HH}_{10\times4}} & 0_{10\times8} & \mathcal{M}^{\chi\chi}_{\chi\chi_{10\times10}}\end{pmatrix}, \tag{C8}$$

where

$$\mathcal{M}^{\rm HH}_{{\rm HH}_{4\times4}}=\begin{array}{c}\\ hh/\sqrt{2}\\ G^0G^0/\sqrt{2}\\ G^+G^-\\ hG^0\end{array}\begin{array}{c}\begin{array}{cccc}hh/\sqrt{2} & G^0G^0/\sqrt{2} & G^+G^- & hG^0\end{array}\\ \begin{pmatrix}3\lambda_H & \lambda_H & \sqrt{2}\lambda_H & 0\\ \lambda_H & 3\lambda_H & \sqrt{2}\lambda_H & 0\\ \sqrt{2}\lambda_H & \sqrt{2}\lambda_H & 4\lambda_H & 0\\ 0 & 0 & 0 & 2\lambda_H\end{pmatrix}\end{array}, \tag{C9}$$

$$\mathcal{M}^{\rm H\chi}_{{\rm H}\chi_{8\times8}}=\begin{array}{c}\\ h\chi_1\\ h\chi_1^*\\ h\chi_2\\ h\chi_2^*\\ G^0\chi_1\\ G^0\chi_1^*\\ G^0\chi_2\\ G^0\chi_2^*\end{array}\begin{array}{c}\begin{array}{cccccccc}h\chi_1 & h\chi_1^* & h\chi_2 & h\chi_2^* & G^0\chi_1 & G^0\chi_1^* & G^0\chi_2 & G^0\chi_2^*\end{array}\\ \begin{pmatrix}0 & \lambda_{1H} & \lambda_{12H}/2 & 0 & 0 & 0 & 0 & 0\\ \lambda_{1H} & 0 & 0 & \lambda_{12H}/2 & 0 & 0 & 0 & 0\\ \lambda_{12H}/2 & 0 & 0 & \lambda_{2H} & 0 & 0 & 0 & 0\\ 0 & \lambda_{12H}/2 & \lambda_{2H} & 0 & 0 & 0 & 0 & 0\\ 0 & 0 & 0 & 0 & 0 & \lambda_{1H} & \lambda_{12H}/2 & 0\\ 0 & 0 & 0 & 0 & \lambda_{1H} & 0 & 0 & \lambda_{12H}/2\\ 0 & 0 & 0 & 0 & \lambda_{12H}/2 & 0 & 0 & \lambda_{2H}\\ 0 & 0 & 0 & 0 & 0 & \lambda_{12H}/2 & \lambda_{2H} & 0\end{pmatrix}\end{array}, \tag{C10}$$

$$\mathcal{M}^{\chi\chi}_{{\rm HH}_{10\times4}}=\begin{array}{c}\\ \chi_1\chi_1/\sqrt{2}\\ \chi_1^*\chi_1^*/\sqrt{2}\\ \chi_2\chi_2/\sqrt{2}\\ \chi_2^*\chi_2^*/\sqrt{2}\\ \chi_1\chi_1^*\\ \chi_2\chi_2^*\\ \chi_1\chi_2\\ \chi_1^*\chi_2^*\\ \chi_1\chi_2^*\\ \chi_1^*\chi_2\end{array}\begin{array}{c}\begin{array}{cccc}hh/\sqrt{2} & G^0G^0/\sqrt{2} & G^+G^- & hG^0\end{array}\\ \begin{pmatrix}0 & 0 & 0 & 0\\ 0 & 0 & 0 & 0\\ 0 & 0 & 0 & 0\\ 0 & 0 & 0 & 0\\ \lambda_{1H}/\sqrt{2} & \lambda_{1H}/\sqrt{2} & \lambda_{1H} & 0\\ \lambda_{2H}/\sqrt{2} & \lambda_{2H}/\sqrt{2} & \lambda_{2H} & 0\\ \lambda_{12H}/(2\sqrt{2}) & \lambda_{12H}/(2\sqrt{2}) & \lambda_{12H}/2 & 0\\ \lambda_{12H}/(2\sqrt{2}) & \lambda_{12H}/(2\sqrt{2}) & \lambda_{12H}/2 & 0\\ 0 & 0 & 0 & 0\\ 0 & 0 & 0 & 0\end{pmatrix}\end{array}, \tag{C11}$$

$$\mathcal{M}^{\chi\chi}_{\chi\chi_{10\times10}} = \begin{array}{c} \\ \chi_1\chi_1/\sqrt{2} \\ \chi_1^*\chi_1^*/\sqrt{2} \\ \chi_2\chi_2/\sqrt{2} \\ \chi_2^*\chi_2^*/\sqrt{2} \\ \chi_1\chi_1^* \\ \chi_2\chi_2^* \\ \chi_1\chi_2 \\ \chi_1^*\chi_2^* \\ \chi_1\chi_2^* \\ \chi_1^*\chi_2 \end{array} \begin{array}{c} \begin{array}{cccccccccc} \chi_1\chi_1/\sqrt{2} & \chi_1^*\chi_1^*/\sqrt{2} & \chi_2\chi_2/\sqrt{2} & \chi_2^*\chi_2^*/\sqrt{2} & \chi_1\chi_1^* & \chi_2\chi_2^* & \chi_1\chi_2 & \chi_1^*\chi_2^* & \chi_1\chi_2^* & \chi_1^*\chi_2 \end{array} \\ \begin{pmatrix} 0 & 2\lambda_{\chi_1} & \lambda'_{12} & 0 & 0 & 0 & 0 & 0 & 0 & \lambda_3/\sqrt{2} \\ 2\lambda_{\chi_1} & 0 & 0 & \lambda'_{12} & 0 & 0 & 0 & 0 & \lambda_3/\sqrt{2} & 0 \\ \lambda'_{12} & 0 & 0 & 2\lambda_{\chi_2} & 0 & 0 & 0 & 0 & \lambda_4/\sqrt{2} & 0 \\ 0 & \lambda'_{12} & 2\lambda_{\chi_2} & 0 & 0 & 0 & 0 & 0 & 0 & \lambda_4/\sqrt{2} \\ 0 & 0 & 0 & 0 & 4\lambda_{\chi_1} & \lambda_{12} & \lambda_3 & \lambda_3 & 0 & 0 \\ 0 & 0 & 0 & 0 & \lambda_{12} & 4\lambda_{\chi_2} & \lambda_4 & \lambda_4 & 0 & 0 \\ 0 & 0 & 0 & 0 & \lambda_3 & \lambda_4 & 2\lambda'_{12} & \lambda_{12} & 0 & 0 \\ 0 & 0 & 0 & 0 & \lambda_3 & \lambda_4 & \lambda_{12} & 2\lambda'_{12} & 0 & 0 \\ 0 & \frac{\lambda_3}{\sqrt{2}} & \frac{\lambda_4}{\sqrt{2}} & 0 & 0 & 0 & 0 & 0 & 0 & \lambda_{12} \\ \frac{\lambda_3}{\sqrt{2}} & 0 & 0 & \frac{\lambda_4}{\sqrt{2}} & 0 & 0 & 0 & 0 & \lambda_{12} & 0 \end{pmatrix} \end{array},$$

$$\mathcal{M}^{\mathrm{SC}}_{6\times6} = \begin{array}{c} \\ |hG^+\rangle \\ |G^0G^+\rangle \\ |\chi_1G^+\rangle \\ |\chi_1^*G^+\rangle \\ |\chi_2G^+\rangle \\ |\chi_2^*G^+\rangle \end{array} \begin{array}{c} \begin{array}{cccccc} |hG^+\rangle & |G^0G^+\rangle & |\chi_1G^+\rangle & |\chi_1^*G^+\rangle & |\chi_2G^+\rangle & |\chi_2^*G^+\rangle \end{array} \\ \begin{pmatrix} 2\lambda_H & 0 & 0 & 0 & 0 & 0 \\ 0 & 2\lambda_H & 0 & 0 & 0 & 0 \\ 0 & 0 & 0 & \lambda_{1H} & \lambda_{12H}/2 & 0 \\ 0 & 0 & \lambda_{1H} & 0 & 0 & \lambda_{12H}/2 \\ 0 & 0 & \lambda_{12H}/2 & 0 & 0 & \lambda_{2H} \\ 0 & 0 & 0 & \lambda_{12H}/2 & \lambda_{2H} & 0 \end{pmatrix} \end{array}, \tag{C12}$$

$$\mathcal{M}^{\mathrm{DC}}_{1\times1} = \begin{array}{c} \\ \frac{1}{\sqrt{2}}|G^+G^+\rangle \end{array} \begin{array}{c} \begin{array}{c} \frac{1}{\sqrt{2}}|G^+G^+\rangle \end{array} \\ \begin{pmatrix} 2\lambda_H \end{pmatrix} \end{array}. \tag{C13}$$

After determining the eigenvalues of Eq. (C7), we conclude that the tree-level unitarity constraints in this setup are as follows:

$$|\lambda_H| \leq 4\pi, \tag{C14}$$

$$|\lambda_{12} - 2\lambda'_{12}| \leq 8\pi, \tag{C15}$$

$$|\lambda_{1H} + \lambda_{2H} \pm \sqrt{(\lambda_{1H} - \lambda_{2H})^2 + \lambda_{12H}^2}| \leq 16\pi. \tag{C16}$$

The other ten distinct eigenvalues, along with their corresponding unitarity constraints, can be obtained by solving the remaining eigenvalue equations of the matrix in Eq. (C7). These lengthy results are omitted here, but all unitarity constraints have been carefully evaluated and numerically verified in our analysis.

APPENDIX D: RELEVANT FEYNMAN DIAGRAMS FOR TWO-COMPONENT DM IN THE $\mathcal{Z}_3$ SCENARIO

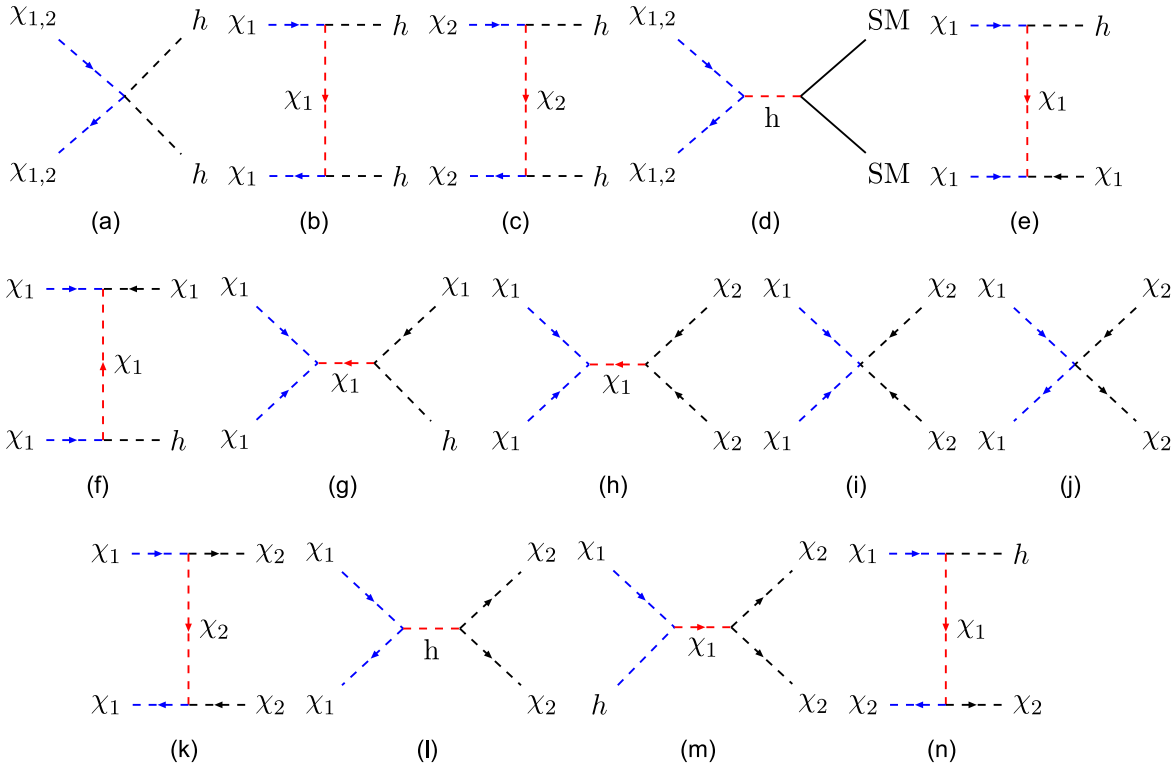


FIG. 12. The Feynman diagrams in panels (a) to (d) represent the self-annihilation of χ_1 and χ_2 DM, where SM $= \{$Higgs, quarks, leptons, $W^{\pm}$, and Z boson$\}$. The Feynman diagrams in panels (e) to (g), (h) to (l), and (m) and (n) represent the semiannihilation, conversion, and semiconversion channels of χ_1 relevant for scenarios A and B.

[1] F. Zwicky, Die Rotverschiebung von extragalaktischen nebeln, Helv. Phys. Acta **6**, 110 (1933).
[2] F. Zwicky, On the masses of nebulae and of clusters of nebulae, Astrophys. J. **86**, 217 (1937).
[3] T. S. van Albada, J. N. Bahcall, K. Begeman, and R. Sancisi, The distribution of dark matter in the spiral galaxy NGC-3198, Astrophys. J. **295**, 305 (1985).
[4] V. Trimble, Existence and nature of dark matter in the universe, Annu. Rev. Astron. Astrophys. **25**, 425 (1987).
[5] Y. Sofue, Y. Tutui, M. Honma, A. Tomita, T. Takamiya, J. Koda, and Y. Takeda, Central rotation curves of spiral galaxies, Astrophys. J. **523**, 136 (1999).
[6] Y. Sofue and V. Rubin, Rotation curves of spiral galaxies, Annu. Rev. Astron. Astrophys. **39**, 137 (2001).
[7] D. Clowe, M. Bradac, A. H. Gonzalez, M. Markevitch, S. W. Randall, C. Jones, C. Jones, and D. Zaritsky, A direct empirical proof of the existence of dark matter, Astrophys. J. Lett. **648**, L109 (2006).
[8] M. Girardi, R. Barrena, W. Boschin, and E. Ellingson, Cluster Abell 520: A perspective based on member galaxies. A cluster forming at the crossing of three filaments?, Astron. Astrophys. **491**, 379 (2008).
[9] M. Girardi, W. Boschin, F. Gastaldello, G. Giovannini, F. Govoni, M. Murgia, R. Barrena, S. Ettori, M. Trasatti, and V. Vacca, A multiwavelength view of the galaxy cluster Abell 523 and its peculiar diffuse radio source, Mon. Not. R. Astron. Soc. **456**, 2829 (2016).
[10] T. Dacunha, M. Belyakov, S. Adhikari, T.-h. Shin, S. Goldstein, and B. Jain, Connecting galaxy evolution in clusters with their radial profiles and phase space distribution: Results from the IllustrisTNG hydrodynamical simulations, Mon. Not. R. Astron. Soc. **512**, 4378 (2022).
[11] V. Springel and G. Farrar, The speed of the bullet in the merging galaxy cluster 1E0657-56, Mon. Not. R. Astron. Soc. **380**, 911 (2007).
[12] WMAP Science Team Collaboration, Results from the Wilkinson microwave anisotropy probe, Prog. Theor. Exp. Phys. **2014**, 6B102 (2014).
[13] Planck Collaboration, Planck 2018 results. VI. Cosmological parameters, Astron. Astrophys. **641**, A6 (2020).

[14] D. Clowe, A. Gonzalez, and M. Markevitch, Weak lensing mass reconstruction of the interacting cluster 1E0657-558: Direct evidence for the existence of dark matter, Astrophys. J. **604**, 596 (2004).
[15] M. Markevitch, A. H. Gonzalez, D. Clowe, A. Vikhlinin, L. David, W. Forman, C. Jones, S. Murray, and W. Tucker, Direct constraints on the dark matter self-interaction cross-section from the merging galaxy cluster 1E0657-56, Astrophys. J. **606**, 819 (2004).
[16] S. W. Randall, M. Markevitch, D. Clowe, A. H. Gonzalez, and M. Bradac, Constraints on the self-interaction cross-section of dark matter from numerical simulations of the merging galaxy cluster 1E 0657-56, Astrophys. J. **679**, 1173 (2008).
[17] F. Kahlhoefer, K. Schmidt-Hoberg, J. Kummer, and S. Sarkar, On the interpretation of dark matter self-interactions in Abell 3827, Mon. Not. R. Astron. Soc. **452**, L54 (2015).
[18] P. Gondolo and G. Gelmini, Cosmic abundances of stable particles: Improved analysis, Nucl. Phys. **B360**, 145 (1991).
[19] C. Balázs, T. Li, and J. L. Newstead, Thermal dark matter implies new physics not far above the weak scale, J. High Energy Phys. 08 (2014) 061.
[20] C. E. Yaguna, The singlet scalar as FIMP dark matter, J. High Energy Phys. 08 (2011) 060.
[21] H. Baer, K.-Y. Choi, J. E. Kim, and L. Roszkowski, Dark matter production in the early Universe: Beyond the thermal WIMP paradigm, Phys. Rep. **555**, 1 (2015).
[22] A. Biswas and A. Gupta, Calculation of momentum distribution function of a non-thermal fermionic dark matter, J. Cosmol. Astropart. Phys. 03 (2017) 033.
[23] N. Bernal, M. Heikinheimo, T. Tenkanen, K. Tuominen, and V. Vaskonen, The dawn of FIMP dark matter: A review of models and constraints, Int. J. Mod. Phys. A **32**, 1730023 (2017).
[24] D. Curtin *et al.*, Long-lived particles at the energy frontier: The MATHUSLA physics case, Rep. Prog. Phys. **82**, 116201 (2019).
[25] N. Chakrabarty, P. Konar, R. Roshan and, and S. Show, Thermally corrected masses and freeze-in dark matter: A case study, Phys. Rev. D **107**, 035021 (2023).
[26] Y. Hochberg, E. Kuflik, T. Volansky, and J. G. Wacker, Mechanism for thermal relic dark matter of strongly interacting massive particles, Phys. Rev. Lett. **113**, 171301 (2014).
[27] Y. Hochberg, E. Kuflik, H. Murayama, T. Volansky, and J. G. Wacker, Model for thermal relic dark matter of strongly interacting massive particles, Phys. Rev. Lett. **115**, 021301 (2015).
[28] Y. Hochberg, E. Kuflik, and H. Murayama, SIMP spectroscopy, J. High Energy Phys. 05 (2016) 090.
[29] S. Tulin and H.-B. Yu, Dark matter self-interactions and small scale structure, Phys. Rep. **730**, 1 (2018).
[30] S.-M. Choi, H. M. Lee, P. Ko, and A. Natale, Resolving phenomenological problems with strongly-interacting-massive-particle models with dark vector resonances, Phys. Rev. D **98**, 015034 (2018).
[31] S. Bhattacharya, P. Ghosh, and S. Verma, SIMPler realisation of scalar dark matter, J. Cosmol. Astropart. Phys. 01 (2020) 040.
[32] M. Cirelli, N. Fornengo, B. J. Kavanagh, and E. Pinetti, Integral x-ray constraints on sub-GeV dark matter, Phys. Rev. D **103**, 063022 (2021).
[33] B. Barman and N. Bernal, Gravitational SIMPs, J. Cosmol. Astropart. Phys. 06 (2021) 011.
[34] A. Kamada, S. Kobayashi, and T. Kuwahara, Perturbative unitarity of strongly interacting massive particle models, J. High Energy Phys. 02 (2023) 217.
[35] S. Bhattacharya, P. Poulose, and P. Ghosh, Multipartite interacting scalar dark matter in the light of updated LUX data, J. Cosmol. Astropart. Phys. 04 (2017) 043.
[36] A. Dutta Banik, M. Pandey, D. Majumdar, and A. Biswas, Two component WIMP–FImP dark matter model with singlet fermion, scalar and pseudo scalar, Eur. Phys. J. C **77**, 657 (2017).
[37] S. Bhattacharya, S. Chakraborti, and D. Pradhan, Electroweak symmetry breaking and WIMP-FIMP dark matter, J. High Energy Phys. 07 (2022) 091.
[38] S.-Y. Ho, P. Ko, and C.-T. Lu, Scalar and fermion two-component SIMP dark matter with an accidental $\mathbb{Z}_4$ symmetry, J. High Energy Phys. 03 (2022) 005.
[39] S.-M. Choi, J. Kim, P. Ko, and J. Li, A multi-component SIMP model with $\mathrm{U}(1)_X \to \mathrm{Z}_2 \times \mathrm{Z}_3$, J. High Energy Phys. 09 (2021) 028.
[40] M. Pandey, D. Majumdar, and K. P. Modak, Two component feebly interacting massive particle (FIMP) dark matter, J. Cosmol. Astropart. Phys. 06 (2018) 023.
[41] S. Peyman Zakeri, S. Mohammad Moosavi Nejad, M. Zakeri, and S. Yaser Ayazi, A minimal model for two-component FIMP dark matter: A basic search, Chin. Phys. C **42**, 073101 (2018).
[42] S. Bhattacharya, D. Pradhan, and J. Lahiri, Dynamics of pseudofeebly interacting massive particles in presence of thermal dark matter, Phys. Rev. D **108**, L111702 (2023).
[43] S. Bhattacharya, J. Lahiri, and D. Pradhan, Detection possibility of a pseudo-FIMP in the presence of a thermal WIMP, Phys. Rev. D **109**, 095031 (2024).
[44] PandaX Collaboration, Search for dark-matter–nucleon interactions with a dark mediator in PandaX-4T, Phys. Rev. Lett. **131**, 191002 (2023).
[45] XENON Collaboration, First dark matter search with nuclear recoils from the XENONnT experiment, Phys. Rev. Lett. **131**, 041003 (2023).
[46] LZ Collaboration, First dark matter search results from the LUX-ZEPLIN (LZ) experiment, Phys. Rev. Lett. **131**, 041002 (2023).
[47] L. Baudis, DARWIN/XLZD: A future xenon observatory for dark matter and other rare interactions, Nucl. Phys. **B1003**, 116473 (2024).
[48] Fermi-LAT Collaboration, Searching for dark matter annihilation from Milky Way dwarf spheroidal galaxies with six years of Fermi large area telescope data, Phys. Rev. Lett. **115**, 231301 (2015).
[49] Fermi-LAT Collaboration, Sensitivity projections for dark matter searches with the Fermi large area telescope, Phys. Rep. **636**, 1 (2016).

[50] Fermi-LAT, DES Collaboration, Searching for dark matter annihilation in recently discovered Milky Way satellites with Fermi-LAT, Astrophys. J. **834**, 110 (2017).
[51] H.E.S.S. Collaboration, Search for dark matter annihilations towards the inner Galactic halo from 10 years of observations with H.E.S.S, Phys. Rev. Lett. **117**, 111301 (2016).
[52] CTAO Collaboration, Dark matter line searches with the Cherenkov telescope array, J. Cosmol. Astropart. Phys. 07 (2024) 047.
[53] B. S. Acharya *et al.* (CTA Consortium Collaboration), *Science with the Cherenkov Telescope Array* (World Scientific Publishing, Singapore, 2018), 10.1142/10986.
[54] CTA Collaboration, Sensitivity of the Cherenkov telescope array to a dark matter signal from the Galactic Centre, J. Cosmol. Astropart. Phys. 01 (2021) 057.
[55] H. Silverwood, C. Weniger, P. Scott, and G. Bertone, A realistic assessment of the CTA sensitivity to dark matter annihilation, J. Cosmol. Astropart. Phys. 03 (2015) 055.
[56] K. M. Zurek, Multi-component dark matter, Phys. Rev. D **79**, 115002 (2009).
[57] S. Profumo, K. Sigurdson, and L. Ubaldi, Can we discover multi-component WIMP dark matter?, J. Cosmol. Astropart. Phys. 12 (2009) 016.
[58] M. V. Medvedev, Cosmological simulations of multi-component cold dark matter, Phys. Rev. Lett. **113**, 071303 (2014).
[59] L. Bian, R. Ding, and B. Zhu, Two component Higgs-portal dark matter, Phys. Lett. B **728**, 105 (2014).
[60] S. Bhattacharya, A. Drozd, B. Grzadkowski, and J. Wudka, Two-component dark matter, J. High Energy Phys. 10 (2013) 158.
[61] S. Esch, M. Klasen, and C. E. Yaguna, A minimal model for two-component dark matter, J. High Energy Phys. 09 (2014) 108.
[62] M. Aoki and T. Toma, Implications of two-component dark matter induced by forbidden channels and thermal freeze-out, J. Cosmol. Astropart. Phys. 01 (2017) 042.
[63] C. E. Yaguna and O. Zapata, Multi-component scalar dark matter from a Z_N symmetry: A systematic analysis, J. High Energy Phys. 03 (2020) 109.
[64] C. E. Yaguna and O. Zapata, Two-component scalar dark matter in Z_{2n} scenarios, J. High Energy Phys. 10 (2021) 185.
[65] C. E. Yaguna and O. Zapata, Fermion and scalar two-component dark matter from a Z4 symmetry, Phys. Rev. D **105**, 095026 (2022).
[66] G. Bélanger, A. Pukhov, C. E. Yaguna, and O. Zapata, The Z_5 model of two-component dark matter, J. High Energy Phys. 09 (2020) 030.
[67] G. Bélanger, K. Kannike, A. Pukhov, and M. Raidal, Minimal semi-annihilating $\mathbb{Z}_N$ scalar dark matter, J. Cosmol. Astropart. Phys. 06 (2014) 021.
[68] X. Qi and H. Sun, Inflation and dark matter in the Z_5 model, J. Cosmol. Astropart. Phys. 05 (2023) 051.
[69] J. McDonald, Gauge singlet scalars as cold dark matter, Phys. Rev. D **50**, 3637 (1994).
[70] C. P. Burgess, M. Pospelov, and T. ter Veldhuis, The minimal model of nonbaryonic dark matter: A singlet scalar, Nucl. Phys. **B619**, 709 (2001).
[71] W.-L. Guo and Y.-L. Wu, The real singlet scalar dark matter model, J. High Energy Phys. 10 (2010) 083.
[72] S. Profumo, L. Ubaldi, and C. Wainwright, Singlet scalar dark matter: Monochromatic gamma rays and metastable vacua, Phys. Rev. D **82**, 123514 (2010).
[73] A. Djouadi, A. Falkowski, Y. Mambrini, and J. Quevillon, Direct detection of Higgs-portal dark matter at the LHC, Eur. Phys. J. C **73**, 2455 (2013).
[74] J. M. Cline, K. Kainulainen, P. Scott, and C. Weniger, Update on scalar singlet dark matter, Phys. Rev. D **88**, 055025 (2013).
[75] L. Feng, S. Profumo, and L. Ubaldi, Closing in on singlet scalar dark matter: LUX, invisible Higgs decays and gamma-ray lines, J. High Energy Phys. 03 (2015) 045.
[76] M. Duerr, P. Fileviez Perez, and J. Smirnov, Scalar singlet dark matter and gamma lines, Phys. Lett. B **751**, 119 (2015).
[77] H. Han and S. Zheng, New constraints on Higgs-portal scalar dark matter, J. High Energy Phys. 12 (2015) 044.
[78] GAMBIT Collaboration, Status of the scalar singlet dark matter model, Eur. Phys. J. C **77**, 568 (2017).
[79] C. E. Yaguna, Gamma rays from the annihilation of singlet scalar dark matter, J. Cosmol. Astropart. Phys. 03 (2009) 003.
[80] A. Goudelis, Y. Mambrini, and C. Yaguna, Antimatter signals of singlet scalar dark matter, J. Cosmol. Astropart. Phys. 12 (2009) 008.
[81] M. Gonderinger, Y. Li, H. Patel, and M. J. Ramsey-Musolf, Vacuum stability, perturbativity, and scalar singlet dark matter, J. High Energy Phys. 01 (2010) 053.
[82] S. Bhattacharya, P. Ghosh, T. N. Maity, and T. S. Ray, Mitigating direct detection bounds in non-minimal Higgs portal scalar dark matter models, J. High Energy Phys. 10 (2017) 088.
[83] G. Belanger, K. Kannike, A. Pukhov, and M. Raidal, Z_3 scalar singlet dark matter, J. Cosmol. Astropart. Phys. 01 (2013) 022.
[84] P. Athron, J. M. Cornell, F. Kahlhoefer, J. Mckay, P. Scott, and S. Wild, Impact of vacuum stability, perturbativity and XENON1T on global fits of $\mathbb{Z}_2$ and $\mathbb{Z}_3$ scalar singlet dark matter, Eur. Phys. J. C **78**, 830 (2018).
[85] A. Hektor, A. Hryczuk, and K. Kannike, Improved bounds on $\mathbb{Z}_3$ singlet dark matter, J. High Energy Phys. 03 (2019) 204.
[86] K. Kannike, K. Loos, and M. Raidal, Gravitational wave signals of pseudo-Goldstone dark matter in the $\mathbb{Z}_3$ complex singlet model, Phys. Rev. D **101**, 035001 (2020).
[87] P. Ko and Y. Tang, Semi-annihilating Z_3 dark matter for XENON1T excess, Phys. Lett. B **815**, 136181 (2021).
[88] A. Liu, Z.-L. Han, Y. Jin, and H. Li, Sterile neutrino portal dark matter with Z3 symmetry, Phys. Rev. D **108**, 075021 (2023).
[89] F. Kahlhoefer, K. Schmidt-Hoberg, T. Schwetz, and S. Vogl, Implications of unitarity and gauge invariance for simplified dark matter models, J. High Energy Phys. 02 (2016) 016.
[90] M. D. Goodsell and F. Staub, Unitarity constraints on general scalar couplings with SARAH, Eur. Phys. J. C **78**, 649 (2018).

[91] R. N. Lerner and J. McDonald, Gauge singlet scalar as inflaton and thermal relic dark matter, Phys. Rev. D **80**, 123507 (2009).
[92] K. Kannike, Vacuum stability conditions from copositivity criteria, Eur. Phys. J. C **72**, 2093 (2012).
[93] K. Kannike, Vacuum stability of a general scalar potential of a few fields, Eur. Phys. J. C **76**, 324 (2016).
[94] Y. Cai and A. P. Spray, The galactic center excess from $\mathbb{Z}_3$ scalar semi-annihilations, J. High Energy Phys. 06 (2016) 156.
[95] ATLAS Collaboration, Combination of searches for invisible decays of the Higgs boson using 139 fb^{-1} of proton-proton collision data at $s = 13$ TeV collected with the ATLAS experiment, Phys. Lett. B **842**, 137963 (2023).
[96] CMS Collaboration, A search for decays of the Higgs boson to invisible particles in events with a top-antitop quark pair or a vector boson in proton-proton collisions at $\sqrt{s} = 13$TeV, Eur. Phys. J. C **83**, 933 (2023).
[97] Z. Kang, P. Ko, and T. Matsui, Strong first order EWPT & strong gravitational waves in Z_3-symmetric singlet scalar extension, J. High Energy Phys. 02 (2018) 115.
[98] G. Bélanger, A. Pukhov, C. E. Yaguna, and O. Zapata, The Z_7 model of three-component scalar dark matter, J. High Energy Phys. 03 (2023) 100.
[99] G. Bélanger, F. Boudjema, A. Goudelis, A. Pukhov, and B. Zaldivar, MICROMEGAS5.0: Freeze-in, Comput. Phys. Commun. **231**, 173 (2018).
[100] N. D. Christensen and C. Duhr, FeynRules-Feynman rules made easy, Comput. Phys. Commun. **180**, 1614 (2009).
[101] MAGIC and Fermi-LAT Collaborations, Limits to dark matter annihilation cross-section from a combined analysis of MAGIC and Fermi-LAT observations of dwarf satellite galaxies, J. Cosmol. Astropart. Phys. 02 (2016) 039.
[102] T. Abe and R. Sato, Quantum corrections to the spin-independent cross section of the inert doublet dark matter, J. High Energy Phys. 03 (2015) 109.
[103] K. Schmitz, Kinetic mixing in field theory (2009), https://api.semanticscholar.org/CorpusID:251310605.
[104] J. Bijnens, J. Oredsson, and J. Rathsman, Scalar kinetic mixing and the renormalization group, Phys. Lett. B **792**, 238 (2019).
[105] D. Boyanovsky and J. Chen, Kinetic mixing between a Higgs boson and a nearly degenerate dark scalar: Oscillations and displaced vertices, Phys. Rev. D **96**, 096007 (2017).
[106] O. Lebedev and H. M. Lee, Higgs portal inflation, Eur. Phys. J. C **71**, 1821 (2011).
[107] Y. Ema, Higgs scalaron mixed inflation, Phys. Lett. B **770**, 403 (2017).
[108] C. van de Bruck and J. M. Weller, Quintessence dynamics with two scalar fields and mixed kinetic terms, Phys. Rev. D **80**, 123014 (2009).
[109] P. B. Pal, *An Introductory Course of Particle Physics* (CRC Press, 2014), 10.1201/b17199.
[110] Particle Data Group, Review of particle physics, Prog. Theor. Exp. Phys. **2022**, 083C01 (2022).
[111] V. Ilisie, *Concepts in Quantum Field Theory. A Practitioner's Toolkit*, UNITEXT for Physics (Springer, New York, 2016), 10.1007/978-3-319-22966-9.
[112] T. Han, Collider phenomenology: Basic knowledge and techniques, in *Theoretical Advanced Study Institute in Elementary Particle Physics : Physics in $D \geqq 4$* (2005), pp. 407–454, 10.1142/9789812773579_0008.
[113] B. W. Lee, C. Quigg, and H. B. Thacker, Weak interactions at very high-energies: The role of the Higgs boson mass, Phys. Rev. D **16**, 1519 (1977).
[114] S. Kanemura and K. Yagyu, Unitarity bound in the most general two Higgs doublet model, Phys. Lett. B **751**, 289 (2015).
[115] S. De Curtis, S. Moretti, K. Yagyu, and E. Yildirim, Perturbative unitarity bounds in composite two-Higgs doublet models, Phys. Rev. D **94**, 055017 (2016).
[116] M. P. Bento, J. C. Romão, and J. P. Silva, Unitarity bounds for all symmetry-constrained 3HDMs, J. High Energy Phys. 08 (2022) 273.